Check for updates

Scanning probe microscopy

Ke Bian [1], Christoph Gerber[2], Andreas J. Heinrich [3,4], Daniel J. Müller [5], Simon Scheuring [6,7] and Ying Jiang [1,8,9,10] ✉

Abstract | Scanning probe microscopy (SPM), a key invention in nanoscience, has by now been extended to a wide spectrum of basic and applied fields. Its application to basic science led to a paradigm shift in the understanding and perception of matter at its nanoscopic and even atomic levels. SPM uses a sharp tip to physically raster-scan samples and locally collect information from the surface. Various signals can be directly detected by SPM in real space with atomic or nanoscale resolution, which provides insights into the structural, electronic, vibrational, optical, magnetic, (bio)chemical and mechanical properties. This Primer introduces the key aspects and general features of SPM and SPM set-up and variations, with particular focus on scanning tunnelling microscopy and atomic force microscopy. We outline how to conduct SPM experiments, as well as data analysis of SPM imaging, spectroscopy and manipulation. Recent applications of SPM to physics, chemistry, materials science and biology are then highlighted, with representative examples. We outline issues with reproducibility, and standards on open data are discussed. This Primer also raises awareness of the ongoing challenges and possible ways to overcome these difficulties, followed by an outlook of future possible directions.

Tunnelling current
The current created from electrons tunnelling through a finite barrier that is forbidden in the classic regime.

Raster-scanning
A rectangular pattern of image capture and reconstruction.

Tip–sample junction
The tunnelling junction between the tip and the sample where electrons tunnel through a finite barrier in between.

Piezoelectric effect
The effect showing a finite induced voltage on both sides of a material when a specific pressure is applied on it.

Visualizing atoms on a solid surface has been a long-standing dream for researchers, and was finally fulfilled by the invention of scanning tunnelling microscopy (STM) in 1981 by Rohrer, Binnig and Gerber at IBM Zürich[1]. STM uses an atomically sharp biased metal tip to collect tiny currents from the metal surface, based on the quantum mechanical effect termed tunnelling (FIG. 1a). Owing to the highly localized nature of the tunnelling current, atomically resolved images could be obtained by raster-scanning the tip over the surface while using a feedback loop to keep the tunnelling current constant. Soon after the invention of STM, Binnig et al. were able to map the tip–sample interaction by atomic forces instead of the tunnelling current, which led to the birth of atomic force microscopy (AFM)[2] (FIG. 1b). AFM is able to image almost any type of surface, unlike STM that requires conducting or semiconducting samples. AFM and STM take advantage of different feedback signals to maintain the tip–sample interaction, but the basic principle of operation is similar in both techniques and reminiscent of a record player, where a tip senses the surface topography of the sample via physical raster-scanning.

A large family of scanning probe microscopy (SPM) methods have emerged as variations of STM and AFM, by integrating nanosensors on the tip or coupling various electromagnetic waves with the tip–sample junction. The measurable physical quantities range from the electric current, force and capacitance to photons, magnetic/electric field, strain and temperature. The emergence of SPM in the then-fledgling field of nanotechnology changed researchers' perception and understanding of matter at atomic or molecular levels. It doubtlessly opened up new possibilities and avenues in physics, chemistry, materials science, biology and medicine, and stimulates increasing numbers of students and researchers around the world.

SPM would not be possible without the piezoelectric effect, that is, the deformation of materials as the result of applying an electric field. The effect enables scanning with picometre precision by simply applying voltages to piezo elements. The core of the SPM is the scanner, which allows stably approaching the tip to the surface from a macroscopic distance to the nanometre scale. An atomically sharp tip is another key component of SPM ultimately determining the lateral resolution. In addition, vibrational isolation and high-gain, low-noise signal amplifiers are also critical for achieving a sufficiently high signal to noise ratio to ensure atomically resolved images by SPM.

This Primer starts by introducing the technical aspects of SPM (Experimentation) and the general features of SPM data (Results). The applications of SPM to physics, chemistry, materials science and biology are then highlighted with some representative examples (Applications). Afterwards, we discuss issues with reproducibility and field standards on open data (Reproducibility and data deposition). We also point out the limitations of SPM and possible ways to overcome those difficulties (Limitations and optimizations). Finally, some possible future directions of SPM are envisaged (Outlook).

Author addresses

[1]International Center for Quantum Materials, School of Physics, Peking University, Beijing, P. R. China.

[2]Swiss Nanoscience Institute (SNI), Institute of Physics, University of Basel, Basel, Switzerland.

[3]Center for Quantum Nanoscience, Institute for Basic Science (IBS), Seoul, Republic of Korea.

[4]Department of Physics, Ewha Womans University, Seoul, Republic of Korea.

[5]Department of Biosystems Science and Engineering, Eidgenössische Technische Hochschule (ETH) Zürich, Basel, Switzerland.

[6]Department of Anesthesiology, Weill Cornell Medicine, New York, NY, USA.

[7]Department of Physiology and Biophysics, Weill Cornell Medicine, New York, NY, USA.

[8]Collaborative Innovation Center of Quantum Matter, Beijing, P. R. China.

[9]Interdisciplinary Institute of Light-Element Quantum Materials and Research Center for Light-Element Advanced Materials, Peking University, Beijing, P. R. China.

[10]CAS Center for Excellence in Topological Quantum Computation, University of Chinese Academy of Sciences, Beijing, P. R. China.

Experimentation

In this section, we introduce the basics of STM and AFM experimental set-ups, including the key components to achieve high spatial resolution, the working principle and a guide to conduct SPM experiments. We also introduce some representative SPM variations based on STM and AFM, which can map out various physical quantities besides current and force. The sensing mechanism, advantages and applications of those SPM variations are briefly discussed.

Scanning tunnelling microscopy

STM has at its heart a very simple idea: a metal needle that is sharpened to a single atom is approached very close to a surface while a biased voltage between the tip and the surface is applied. When the tip–sample distance reaches the atomic-scale range, some electrons will jump between the tip and the sample, known as the tunnelling current. The tunnelling current is sensitive to the tip–sample distance; it has exponential dependence on the tip–sample distance. For example, in a clean vacuum tunnel junction, the tunnelling current decreases by a factor of ten when the tip–sample distance increases by 0.1 nm (the typical tip–sample distance is in the range 0.3–1 nm). This effect gives STM its atomic-scale lateral spatial resolution as the majority of the tunnelling current stems from only the last atom of the tip apex[3] (FIG. 1a).

The STM tip is usually attached to piezoelectric control elements that allow the tip to be moved with atomic-scale precision (FIG. 2a,b). In almost all STM systems, the tip and the sample should be replaced with new ones in a convenient manner without violently changing the STM configuration. Generally, STMs are very sensitive to noise, which includes electronic noise and vibrational noise from the laboratory environment. Here, we focus on controlling some of these noise sources, from large to atomic scale. The scanner head of the microscope, or the STM body, has macroscopic dimensions typically in the range of a few centimetres. By contrast, the tip–sample distance is often smaller than 1 nm. Ideally, the tip–sample distance is kept stable at approximately 1 pm. As the tunnelling current is sensitive to the tip–sample distance (and, hence, to fluctuations in this distance), mechanical shaking causes noise in the

tunnelling current. Vibrational noise, such as shaking of the laboratory floor and/or the vacuum chambers, must be reduced. The STM system must be built with a rigid scanner head that minimizes changes to the tip–sample distance, as some external shaking of the scanner head is unavoidable. Therefore, the equipment should be kept on a very quiet laboratory floor, usually the basement of the building. The lowest vibration levels are achieved in custom facilities built using heavy (100 ton) concrete blocks floating on special air springs, for example, at the Precision Laboratory of the Max Planck Institute for Solid State Research[4]. A custom building with a heavy concrete floor that is isolated from other buildings can also provide low vibration levels. However, even a well-built general laboratory building can have low levels of vibration below 10 Hz (the IBM Almaden laboratory), despite the increased floor-level vibrations above 10 Hz (FIG. 2c).

Quiet laboratory space must be complemented with a rigid STM scanner design with high mechanical resonance frequencies (FIG. 2b), which makes the microscope resistant against low-frequency shaking. In practice, the lowest frequencies of the STM scan head are found at 1–5 kHz; such a scan head is good at rejecting low-frequency vibrational noise from the building but it is important to limit higher-frequency mechanical noise sources, which can be effectively reduced by soft springs combined with eddy current damping (FIG. 2a). In practice, a properly built scanner head in a low-noise laboratory can reduce tip–sample shaking well below 1 pm, which limits the fluctuation of the detected tunnel current within several per cent.

It is seemingly an impossible task to move the STM tip by atomic-scale dimensions without adding noise, but this has been made possible with the use of piezoelectric materials such as lead zirconate or lead titanate ceramics[1]. A typical piezoelectric material used in STM will change its size by about 1 nm when a voltage of 1 V is applied across its sides[1]. Hence, stable high-voltage sources can hold the tip stable to better than 1 pm while allowing a maximum scan range around 1 μm. However, as for STM systems under ultra-high vacuum (UHV) conditions, it is necessary to change samples without opening the vacuum chamber. The tip must be moved at least 1 mm away from the sample before the sample can be extracted. Although piezoelectric materials are good at atomic-scale length changes, they cannot provide such large displacements; instead, this task is achieved by the coarse approach mechanism with a type of piezo motor, which is the kernel component of the STM scanner head (FIG. 2b). The action of such a motor can be easily visualized: the tip is held on a body — often made from a ceramic — which is mounted on piezoelectric materials. When the piezo materials move slowly, the ceramic body will follow. However, when the piezo materials move rapidly (>100 nm in 10 μs), the body will hold still owing to its inertia. Each step gives a motion in the range of 100 nm. This process can then be repeated many thousands of times to arrive at a macroscopic motion. Such a stick–slip motion[5,6] is reliable in providing coarse motion in the range of a few millimetres, but is among the most difficult parts of STM design as it is

---

Biased voltage
The DC voltage applied to the tunnelling junction, either on the sample or on the tip.

Eddy current
Loops of electrical current induced within a conductor by changing the magnetic field through this conductor based on Faraday's law of induction.

challenging to provide a rigid enough movable motor with mechanical resonance frequency larger than several kilohertz. The well-known types of motor for the coarse approach include the louse type[7], beetle type[5], Pan type[6] and various single-tube types.

There is no way to sharpen the tip to a single atom, and so in situ protocols have been developed for this task. Most often, we start with either a cut platinum/iridium wire or with an etched tungsten wire[8]. A cut wire has the advantage of fewer oxide films on its surface, whereas an etched tip has a much better macroscopic shape. The platinum/iridium tip can be produced by mechanical cutting or electrochemical etching, whereas the tungsten tip can only be made by etching owing to tungsten's brittleness. For most STM measurements, the overall shape of the tip does not matter as the tunnelling only occurs from the atom or cluster of atoms at the very end of the tip. However, for some applications — most notably optical experiments — the macroscopic shape can have a pronounced effect on the plasmonic enhancement of Raman scattering and fluorescence[9].

Lower temperatures are desirable for STM because of improved stability compared with room temperature, as well as higher energy resolution owing to the smaller thermal broadening of the electrons in both the tip and the sample. Eigler introduced a machine with a stable design operating at about 5 K reaching a tip–sample distance noise below 1 pm, which was used to build quantum corrals[10] and move individual atoms[11,12]. Eventually, lower operating temperatures — down to 10 mK (REF.[13]) — were achieved; such ultra-low-temperature STM is also functional under high magnetic fields up to 30 T (REF.[14]). On the other extreme, STM has been used to image the growth of materials in situ at temperatures up to several hundred degrees Celsius[15]. STM has also been used to study catalytic processes under near-ambient pressures[16]. Whereas operation of STM in air is often complicated owing to the presence of water films on the surfaces of samples, STM can work in a more stable manner at a solid–liquid interface, where both the potential stability and the chemical composition inside the aqueous environments are well controlled[17].

Atomic force microscopy

As STM can only probe conductive surfaces relying on the tunnelling current, AFM was conceived to extend atomic resolution to non-conducting surfaces[2]. The advantage of AFM is that it can be employed in a vacuum, an ambient atmosphere and a liquid, and from high to ultra-low temperatures. AFM shares many basic features and key components with STM, such as the vibrational isolation, scanning process, coarse-approaching mechanism and tip treatments. However, as AFM detects local force instead of the tunnelling current, there are some differences in the signal acquisition and the feedback loop (FIG. 1b). In AFM, a tip is mounted at the end of a flexible cantilever, which deflects linearly with the force applied. Contact mode AFM measures tiny deflections of the scanning cantilever and uses a force-feedback circuit to move the sample or tip held by a piezoelectric element in the z direction (maintaining a constant tip–sample distance) to keep the deflection, and thus the applied force, constant. Plotting the z-direction position (height) of the scanned surface pixel by pixel provides the sample topography. An important development for AFM was the optical lever system[18], which reflects a laser beam on the backside of the cantilever to efficiently magnify the tiny cantilever deflections resulting from the interactions of the tip and the sample (FIG. 3a), thus largely enhancing the signal to noise ratio during data acquisition. An important development towards enabling biological AFM was the invention of a liquid cell in which the cantilever and the sample are immersed in physiological solution[19].

Dynamical AFM uses oscillating cantilevers[20]. Concomitant amplitude modulation modes (for example, 'intermittent contact', 'tapping' or 'oscillating' mode) use feedback controls to oscillate the cantilever at resonant frequency and constant amplitude[21] (FIG. 3b). Other oscillating modes apply frequency (frequency modulation) or phase (phase modulation) for feedback control (FIG. 3b). Such dynamic modes control the tip–sample interaction more gently compared with static AFM modes so that interaction forces are minimized.

Frequency modulation AFM (FM-AFM) is used for UHV and low-temperature physics[22], as well as for biological applications[23]. FM-AFM is usually more
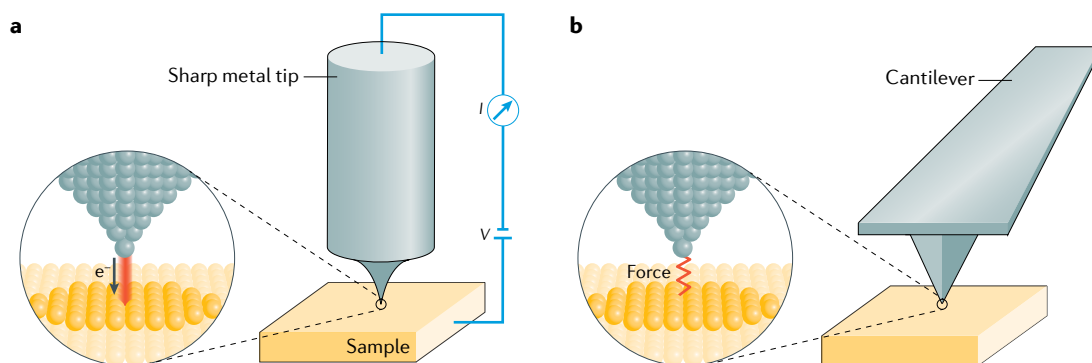

Fig. 1 | **Basic set-up for scanning probe microscopy.** Scanning tunnelling microscopy (STM) and atomic force microscopy (AFM) both use a tip to scan the sample. Both techniques use different feedback signals to maintain constant tip–sample interaction, but their basic principle of operation and image acquisition mechanisms are similar. **a** | STM collects the tunnelling current between the tip apex and the sample when a bias voltage is applied. **b** | AFM detects local forces and corresponding mechanical parameters through a spring-like cantilever.
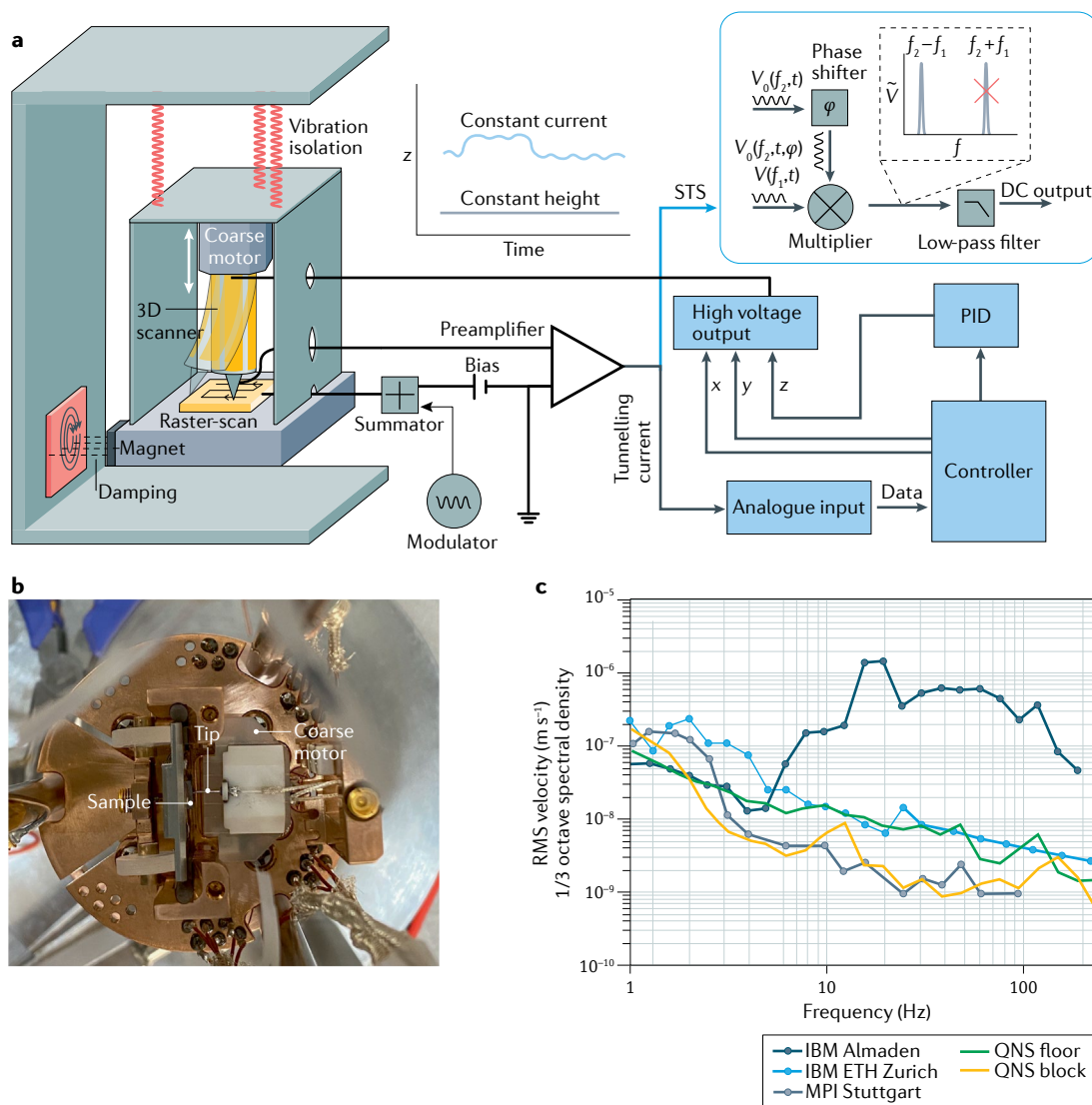
Fig. 2 | **Scanning tunnelling microscopy set-up. a** | Scanning tunnelling microscopy (STM) set-up consisting of a coarse motor, three-dimensional (3D) scanner, vibration isolation device, damping device, preamplifier and controller unit. The frame shields the external electric noise. The proportional integral differential unit (PID) is used for controlling the tip–sample distance in constant current operational mode. Inset: schematic showing lock-in for scanning tunnelling spectroscopy (STS) measurements. The basic electric circuit demonstrates both the process of modulations and its corresponding demodulations, where V is the modulated signal and V_0 is the reference. **b** | Photograph of STM scan head with tip, sample on sample holder and slip–stick walker, all mounted on a metal base plate. **c** | Vibration levels in various STM laboratories from around the world between 1 and 200 Hz. y axis represents the velocity scaled in a fashion typical for architectural comparisons. The lowest vibration levels are dependent on floating concrete blocks (IBM ETH Zurich, MPI Stuttgart, QNS block), high-quality basement levels of laboratory buildings (QNS floor) and regular basement-level laboratory floors (IBM Almaden). RMS, root mean square. Part **c** reprinted with permission from REF.[4], Royal Society of Chemistry.

Temporal resolution
The duration of time for acquisition or capture of a single event in measurements.

Functionalized tips
Modified tips with a single molecule or specific clusters in order to make the tip adapted for specific applications.

precise than amplitude modulation AFM, as the time and frequency can be measured with higher accuracy than amplitude changes. However, force detection by amplitude modulation AFM is simpler and faster, and the amplitude changes with the tip–sample distance in a nearly monotonic manner. Time-lapse AFM imaging can monitor cellular machines at work at the nanoscale level[24]. When using a small cantilever with a high resonant frequency, time-lapse AFM can work at much faster speeds, which allows observation of machinery at a temporal resolution of ~100 ms (REF.[25]); this set-up is known as high-speed AFM.

It is more challenging to obtain high-resolution images in AFM systems, as forces have multiple long-range and short-range components and the force–distance relation between tip and sample can be more complicated than the current–distance relation in STM[26,27]. Presently, subatomic details such as orbitals or chemical bonds can be observed by probing short-range forces with chemically functionalized tips in high vacuum. Meanwhile, researchers developed a plethora of new AFM-based approaches to probe chemical, magnetic and friction forces, and to introduce different spectroscopies such as force spectroscopy with sub-piconewton sensitivity[28,29]

or single-molecule and single-cell force spectroscopy in biology[30–32]. Now, we approach the time at which AFM imaging simultaneously quantifies and structurally maps the various physical, chemical and biological properties of non-living and living objects[24,33,34] (FIG. 3c).

Progress in instrumentation has been key to recent AFM developments. After the quartz tuning fork was first used as the force sensors for non-contact AFM[35], one example of prominent progress is the development of the qPlus sensor, with one prong fixed to enhance the quality factor up to ~100,000 at small amplitude (<50 pm)[28,36]. The qPlus sensor's self-sensing mechanism is enabled by the piezoelectricity of quartz, which converts mechanical deformations into electric signals. Besides the two electrodes used for collecting the induced charges resulting from the deformation, an extra metal line is deposited on the side of the quartz prongs and used for feeding through the tunnelling current, thus allowing simultaneous measurements under STM and AFM modes, where the spatial resolution of AFM has exceeded that of STM.

Imaging, spectroscopy and manipulation

A powerful feature of STM and AFM is the unique capability that imaging, local spectroscopy and manipulation are achieved with atomic-scale spatial resolution, all in the same research tool.

During SPM imaging, the tip height can be controlled by a feedback loop. If the feedback loop is activated, the

corresponding image will be measured at constant current in STM or constant force in AFM. On the other hand, when the feedback is not used, the tip height is kept constant, resulting in the constant-height imaging mode. Under the constant-current/force mode, the tip–sample distance is determined by the preset current/force and typically higher resolution is obtained at smaller tip–sample distance, simultaneously with higher risk of tip damage. By contrast, constant-height imaging only works for flat surfaces, and the results are more straightforward to interpret owing to the absence of the feedback loop, but it suffers from thermal drift between the tip and the specific local structures such as atomic size defects or adsorbed molecules.

Spectroscopic measurements based on SPM can be achieved by fixing the tip at a specific position on the surface and recording the current/force as a function of bias voltage, tip height or time. For scanning tunnelling spectroscopy (STS) of STM, the differential conductance (dI/dV) curve reflects the electronic structure of samples based on the electrons tunnelling to the unoccupied electronic states above the Fermi level or, vice versa, tunnelling from the occupied electronic states below the Fermi level[37]. In some cases, the electrons can tunnel inelastically through the junctions owing to their coupling with vibration, photon–phonon interaction and spin[38,39]. The contribution of those inelastic electrons is usually small compared with the elastic ones and could be more prominent in second-derivative $I(V)$ spectra
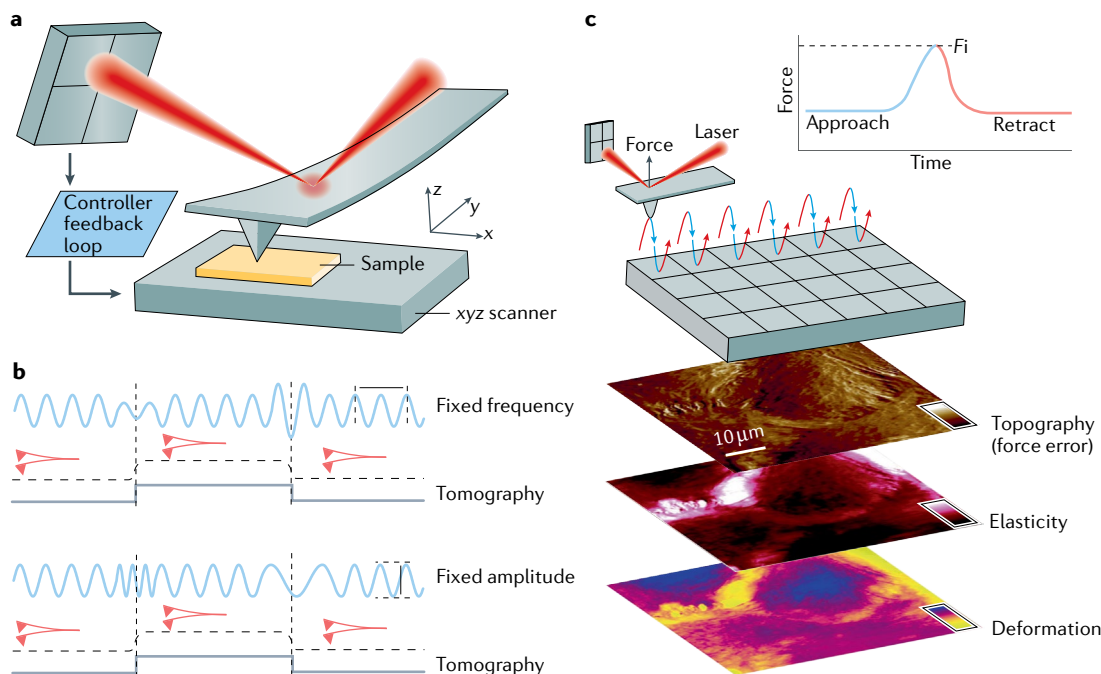

Fig. 3 | **Basics of atomic force microscopy. a** | Laser beam detects cantilever deflection caused by interaction forces between the tip and the sample. Tiny changes in cantilever deflections are compensated by feedback loops controlling the piezoelectric scanner. **b** | Working principles of amplitude modulation atomic force microscopy (AFM) and frequency modulation AFM (FM-AFM). In amplitude modulation AFM, the frequency is fixed, and the amplitude is preset for controlling the tip–sample distance. In FM-AFM, the amplitude is fixed and the phase is locked, whereas the frequency shift is preset for controlling the tip–sample distance. **c** | AFM can record force–distance curves to map mechanical properties of the sample including localized elastic and inelastic deformation, viscoelasticity, energy dissipation, mechanical work, pressure and tension. F_i, indentation force. Part **c** adapted from REF.[34], Springer Nature Limited.

(d^2I/dV^2), such as inelastic electron tunnelling spectroscopy (IETS) (FIG. 4A). To obtain dI/dV and d^2I/dV^2 spectra, a small voltage modulation is added to the bias, and the first-order and second-order components of I–V curves are extracted by lock-in amplifiers (FIG. 2a). In AFM-based force spectroscopy, the tip is approached and withdrawn from a sample surface while recording a force–distance curve (FIG. 4B). The force–distance curves allow analysis of repulsive and adhesive interactions between the tip and the sample, as well as sample deformation and elasticity[40] (BOX 1). AFM can combine imaging with force spectroscopy to simultaneously map mechanical, chemical and biological properties. Therefore, the AFM record for each pixel of the resulting AFM topography represents a force–distance curve, from which multiple parameters such as Young's modulus and energy dissipation, pressures and tension can be extracted (FIG. 3c).

The SPM tip is not only a perfect probe for surface characterization but also acts as a nanoscale hand for manipulating single atoms or molecules[11,41,42]. Precise manipulation is usually achieved through voltage pulses or forces when the tip is positioned directly above the target sites. During such a process, the injected electrons can excite the vibrational modes of atoms or molecules and lead to diffusion, desorption and selective bond breaking or formation[42–44]. For vertical manipulation, an adsorbed molecule is picked up by an STM tip by injecting electrons into the surface, transferred above a target site and then released from the tip by applying a reversed bias voltage, leading to the formation of a new complex[42] (FIG. 4C). For the lateral manipulation, the tip is brought close to the atom or molecule on the surface, such that the tip–sample interaction force is large enough to pull or push the atom or molecule moving over the diffusion barrier[41,45] (FIG. 4D).
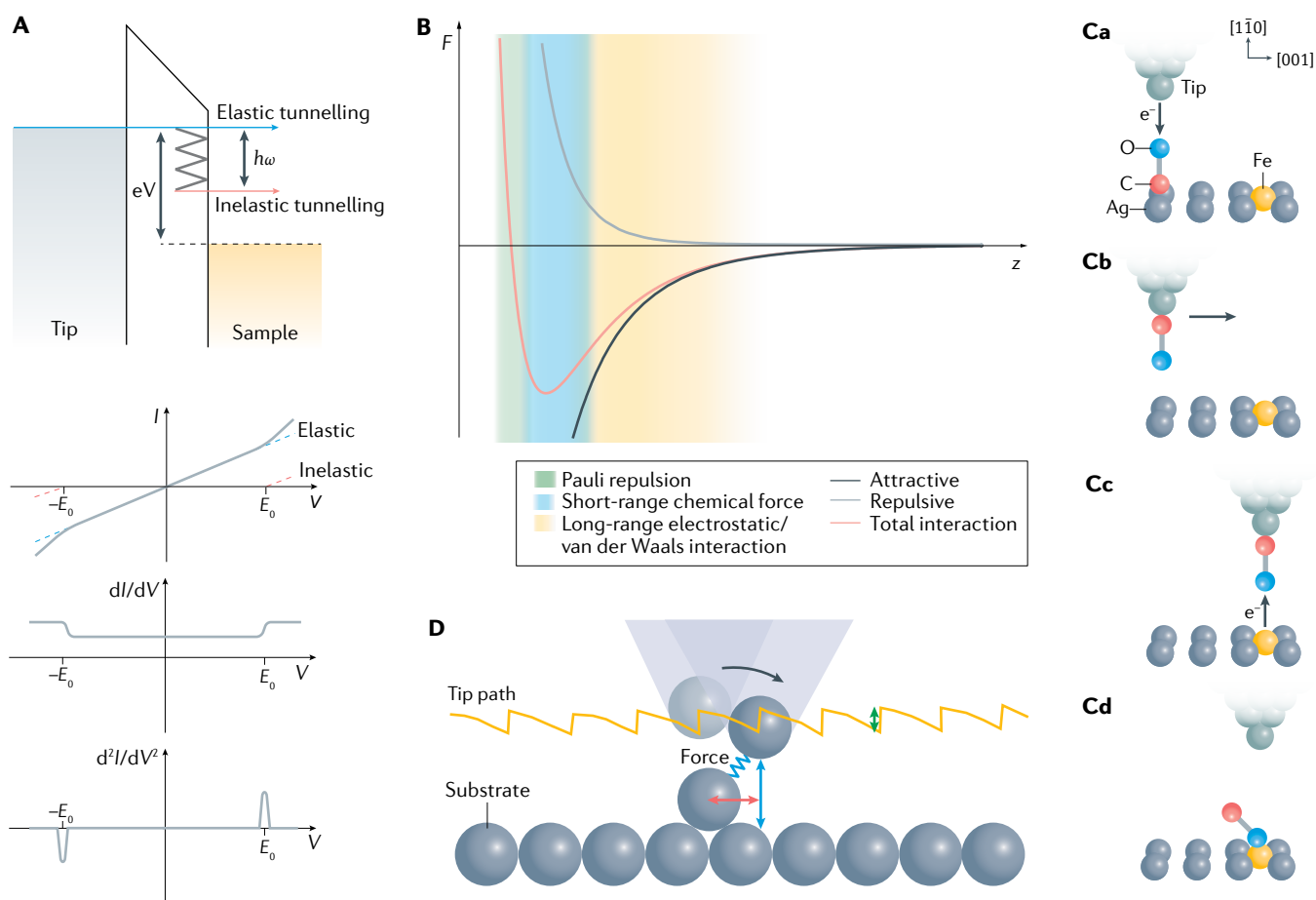

Fig. 4 | **Schematics of scanning probe spectroscopy and manipulations.** **A** | Schematic revealing inelastic tunnelling (red) and elastic tunnelling (blue). Vibrational excitation indicated by wavy lines, which leads to an increase in conductance. Graphs show an I–V curve and corresponding dI/dV and d^2I/dV^2 spectra where extra tunnelling conductance caused by inelastic tunnelling appears at $\pm E_0$. Dashed lines reflect the elastic and inelastic tunnelling channels, whereas solid lines show the actual data. **B** | Schematic showing typical force–distance curves. Both short-range (green region, Pauli repulsion; blue region, short-range chemical force) and long-range (orange region, long-range electrostatic or van der Waals interaction) components are indicated. Black and grey curves represent the attractive force and repulsive force versus tip distance, respectively. **C** | Schematic showing formation of a single bond through scanning tunnelling microscopy. A single molecule can be detached (part **a**), translated (part **b**) and attached onto another adatom through precise manipulation of the scanning tunnelling microscopy (STM) tip (parts **c,d**). **D** | Schematic showing the process of laterally pulling an adatom through the STM tip. Jump height (green arrow), lateral distance between the tip apex and the manipulated adatom (red arrow), and tip height (blue arrow) during manipulation are indicated. Part **C** adapted with permission from REF.[42], AAAS. Part **D** adapted with permission from REF.[41], APS.

Tip preparation and functionalization

Atomically sharp tips are the key to achieving high resolution in SPM. They are usually produced by mechanical cutting or milling, electrochemical etching or more complicated nanofabrication such as focused ion beam systems[46]. However, the tip apex obtained by those methods is not sharp enough for atomically resolved imaging. To obtain an ideal tip terminated with a single atom or a small cluster of atoms, the tip needs to be treated (which includes both sharpening and functionalization) during scanning by poking the tip into the surface and grasping a small cluster of atoms. In STM experiments, the application of high voltages up to 10 V can be used for tip treatment, at a tip–sample distance of ~1 nm to induce field emission[47]. The atoms at the very end of the tip determine the spatial resolution of SPM, not the overall radius of curvature at the apex. In order to obtain high chemical resolution besides topography, one can also evaporate noble metal films such as gold and silver onto the conventional silicon AFM tip; this type of tip has been extensively used for nanoscale chemical analysis under ambient conditions[48,49].

For SPM experiments performed in UHV and low-temperature conditions, the most controllable and precise way to get a well-defined sharp tip is functionalizing the tip apex by picking up a single atom or molecule on the surface[50,51]. Under such conditions, SPM with a CO-functionalized tip can image molecular orbitals[52], owing to the *p*-wave orbitals of the CO molecule. The CO tip also allows access to the short-range Pauli repulsions, reflecting the variations of electron density in individual chemical bonds[53]. As the CO tip has a quadrupole-like charge distribution, it is also sensitive to the high-order electrostatic force[54]. One drawback of the CO tip is the lateral relaxation of the CO molecule at the tip apex, which leads to distortion or even artefacts in the SPM images. Functionalizing the tip at the atomic level, for example replacing the C–O group with oxygen[55] and chlorine[56], yields a more rigid tip with smaller relaxation of the tip apex. However, the resolution of those tips is usually poorer than for the CO tip, as strong relaxation of the CO molecule is also crucial to obtain sharply resolved structural resolution when the tip–sample distance is within the region of Pauli repulsion[57].

For biological AFM imaging applications, tips are typically made of silicon or silicon nitride, which upon exposure to air and immersion into physiological buffer will feature an oxide layer at their surface[58]. To achieve sharper tips with higher aspect ratio, electron beam deposition can be used, resulting in the growth of an amorphous carbon-based apex, which is subsequently rendered hydrophilic using plasma cleaning[59]. Carbon nanotubes have been grafted as a quasi one-dimensional (1D) object at the end of AFM tips to create a super-sharp, very high aspect ratio apex, but despite efforts these tips have so far had no significant impact in the AFM field, likely because of nanotube buckling[60]. Overall for biological imaging applications in liquid, the tip–sample interaction forces range from short range (≈1–10 nm) to long range (>10 nm) and can be composed of a repertoire of different physical, chemical and biological interactions[40]. One approach to study these interactions is to functionalize the AFM tip.

CO-functionalized tip
Modification of the tip with a single CO molecule in order to enhance the spatial resolution of scanning probe microscopy.

Box 1 | **Single-molecule force spectroscopy**

The uniqueness of directly probing physical interactions between the atomic force microscopy (AFM) tip and the biological sample has been exploited to develop single-molecule force spectroscopy. This technique measures the bonds of single receptor–ligand pairs. In the early days of single-molecule force spectroscopy, the AFM tip (or a bead glued to the tip) was functionalized with ligands and the surface of the support, such as a bead on top of the substrate, with receptors[30,288]. If the tip and sample are brought into sufficient proximity, the ligand and receptor can bind. The AFM tip is then withdrawn, and the force required to separate the specific bond is measured. This unbinding force describes the mechanical strength of the receptor–ligand bond. Typically, such experiments are repeated several thousand times to characterize a sufficient number of successful binding and unbinding events. The use of short cantilevers in high-speed AFM set-ups extends the accessible dynamic range in force spectroscopy experiments to measure molecular dynamics simulations[319], whereas low-noise AFMs reach force sensitivity comparable with that of optical tweezers[320].

Variations of SPM

By integrating microsensors on the tip or coupling the electromagnetic waves with different wavelengths into the tip–sample junctions, a large family of SPM methods have been developed since the invention of STM and AFM. In this section, we introduce some representative variations of SPM, which can map out various physical quantities besides current and force, such as magnetic/electric field, photons, strain, temperature, and dielectric and physiological responses. The sensing mechanism, advantages and applications of those SPM variations are briefly discussed in the following sections.

Time-resolved STM. Despite achieving high spatial resolution in real space, one of the most interesting questions about SPM is the speed at which such a device could capture a signal in real time. High-speed image acquisition could be achieved by video-rate STM[15,61], which typically scans a frame within a millisecond timescale. Recently, with the pulsed voltages, fast spin dynamics such as spin relaxation was investigated by electrical pump-probe STM at the level of a single atom[62]. As the bandwidth of the preamplifier and other electronics of SPM is limited to megahertz, ultra-fast dynamics within picoseconds and femtoseconds should be captured by incorporating pump-probe techniques into STM, leading to femtosecond laser STM[63,64] and terahertz STM[65,66]. Examples of various time-resolved STM techniques can be found in TABLE 1.

Magnetic field-sensitive SPM. Magnetic field or spin-sensitive SPM is very useful for characterizing local magnetic structures and spin states in real space (TABLE 2). The simplest method for detecting the local magnetic field is by replacing the conventional non-magnetic probe with a magnetic probe, which is extensively used

Table 1 | **Time-resolved scanning probe microscopy techniques**

Name	Detected signal	Utility	Resolution	Disadvantages and limitations	Refs
Video-rate scanning tunnelling microscopy	Tunnelling current	Fast dynamics during chemical reactions, surface reconstruction and material growth at elevated temperatures	Atomic resolution and millisecond temporal resolution	Spatial resolution is poor owing to short integration time; temporal resolution is limited by the resonance frequency of the scanner and the bandwidth of the electronics	15,61
Electrical pump-probe scanning tunnelling microscopy	Tunnelling current	Fast electron spin dynamics	Atomic resolution and nanosecond temporal resolution	Time resolution is limited by the bandwidth of advanced electronics such as the preamplifier and pulse generators	62
Femtosecond laser scanning tunnelling microscopy	Photo-induced tunnelling current	Ultra-fast charge, spin and phonon dynamics at the atomic scale	Atomic resolution and femtosecond temporal resolution	Laser-induced thermal expansion of the tip can lead to artificial signals	63,64
Terahertz scanning tunnelling microscopy	Photo-induced tunnelling current	Ultra-fast charge, spin and phonon dynamics at the atomic scale	Atomic resolution and femtosecond temporal resolution	Introduction of terahertz light into the ultra-high vacuum and low-temperature scanning tunnelling microscopy system is complicated; the temporal resolution is limited by the wavelength and width of the terahertz pulse	65,66

in magnetic force microscopy[67,68], magnetic exchange force microscopy[69] and spin-polarized STM[70,71]. Another avenue is grafting a micro-magnetic sensor such as a superconducting quantum interference device (SQUID) or Hall probe on the tip, constructing scanning SQUID microscopy[72,73] and scanning Hall probe microscopy[74]. In addition, by incorporating microwaves into SPM to excite magnetic resonance, the magnetic sensitivity of SPM can be enhanced up to single electron or nuclear spin, such as electron spin resonance (ESR) STM[75–77], magnetic resonant force microscopy[78] and nitrogen vacancy-based SPM[79].

Electric field-sensitive SPM. To map out the surface potential or charge with high resolution, typically a conductive SPM tip biased with variable voltage is used (TABLE 3). One form of electric field-sensitive SPM is scanning capacitance microscopy[80], where the local capacitive coupling between the tip and the sample is detected for deriving the local dielectric and electrical properties. Another option for sensing local potential is the integration of a microelectric sensor such as a single-electron transistor onto the tip[81]. For single charge detection, the tip should be brought as close as possible to the sample, which requires a sharp metal tip instead of a microelectric sensor, such as in Kelvin probe force microscopy[82]. Piezoresponse force microscopy (PFM) is another important electric-field sensitive SPM[83,84], in which a modulated pressure is applied locally on the sample by the tip and its piezoelectric response is monitored during scanning.

Liquid-phase SPM. Although surface characterization with atomic resolution is ever-present in UHV and low-temperature experiments, it remains challenging for use in aqueous environments. The self-assembly and reactivity of supramolecular systems inside non-ionic organic liquids has been investigated by liquid-phase STM[85–87]. Meanwhile, working at the solid–electrolyte interfaces, electrochemical STM (EC-STM) is developed with four electrodes including the tip, working electrode, counter electrode and reference electrode, which are controlled by a bipotentiostat[17,88]. As EC-STM only works on conductive surfaces, liquid-phase non-contact AFM was developed for imaging the local structures on insulator–liquid interfaces[89,90]. In order to characterize complex biological systems such as living cells in physiological buffers with high spatial resolution, scanning ion conductance microscopy should be chosen[91]. In this system, the ion current flow from the tip to the reference electrodes in the solution is monitored and used for feedback to control the tip–surface distance. Compared with EC-STM and liquid-phase AFM mentioned above, scanning ion conductance microscopy provides the unique possibility of locally probing the ion transport of biological systems by monitoring the ion current[92]. Similarly, AFM can scan a hollow microcantilever to perform scanning ion conductance microscopy measurements, which is also called fluid force microscopy, to patch clamp or to manipulate living cells[93,94]. Examples of liquid-phase SPM can be found in TABLE 4.

Electrical transport-compatible SPM. In order to make SPM suitable for investigating local electron transport properties both on the surface and the interface of samples such as 2D material-based novel electronic devices, various electrodes should be fabricated on the surface in addition to the bias electrode, acting as source, drain and electric gates. Immediately after the appearance of STM, scanning tunnelling potentiometry was invented

Hall probe
A micron-sized device for detecting the external magnetic field through the Hall effect.

Bipotentiostat
An electronic system capable of controlling two potentiostats, which include two working electrodes, one shared reference electrode and one shared counter electrode for electrochemical measurements.

Table 2 | **Magnetic field-sensitive scanning probe microscopy techniques**

Name	Detected signal	Utility	Resolution and sensitivity	Disadvantages and limitations	Refs
Spin-polarized scanning tunnelling microscopy	Spin-polarized tunnelling current	Nanoscale spin texture or long-range spin ordering of magnetic materials	Atomic resolution with sensitivity of single electron spin	High-energy resolution only works on conductive samples under low temperature and ultra-high vacuum	70,71
Electron spin resonance scanning tunnelling microscopy	Spin-polarized tunnelling current	Spin identification, electron spin resonance spectra/imaging and quantum sensing	Atomic resolution with sensitivity of single electron spin	The spin-polarized tip is not only a probe but has an effect on the coherence of the target spin	75–77
Magnetic force microscopy	Dipolar magnetic interaction	Magnetic structures of sample surfaces	Spatial resolution of several tens of nanometres	The magnetic tip will disturb the magnetic state of the sample, and vice versa, complicating quantitative interpretation of the magnetic force microscopy measurement; atomic resolution cannot be achieved owing to the long-range magnetic forces between tip and sample	67,68
Scanning superconducting quantum interference device microscopy	Magnetic flux and superconducting current	Scanning magnetometry and thermometry at low temperature	Spatial resolution of several tens of nanometres and magnetic sensitivity up to single electron spin	Only works under low temperature; spatial resolution is limited by the size of the superconducting loop	72,73
Nitrogen vacancy centre scanning probe microscopy	Fluorescence of the nitrogen vacancy centre	Scanning magnetometry of nanoscale magnetic textures at various temperatures; compatible with an ambient environment and biological systems	Spatial resolution of ~10 nm and magnetic sensitivity up to single nuclear spin	The quantum sensor is buried underneath the diamond surface, which makes atomic resolution challenging; the shallower nitrogen vacancy has poorer quantum coherence, which decreases the signal to noise ratio and sensitivity	79
Magnetic resonance force microscopy	Magnetic dipolar interaction	Nanoscale electron and nuclear magnetic resonance for structure analysis, especially for biomolecules and particles	Resolution <10 nm and sensitivity up to single nuclear spin	Only works under extremely low temperature; structure of the mechanical sensor is very complex	78
Magnetic exchange force microscopy	Exchange interaction	Nanoscale spin texture or long-range spin ordering of both conductive and non-conductive magnetic materials	Atomic resolution with sensitivity of single electron spin	Spin contrast is lower than that of spin-polarized scanning tunnelling microscopy; requires post-processing for imaging	69
Scanning Hall probe microscopy	Hall current	Quantitative and non-invasive magnetic detection of various magnetic materials	Spatial resolution of several hundreds of nanometres with sensitivity of $1\,nT\,Hz^{-1/2}$	Only works under low temperature in order to suppress the electronic noise; the spatial resolution is limited by the size of the Hall device	74

Table 3 | **Electric field-sensitive scanning probe microscopy techniques**

Name	Detected signal	Utility	Resolution and sensitivity	Disadvantages and limitations	Refs
Scanning single-electron transistor microscopy	Tunnelling current	Local electric field and potential caused by the local charges, especially the local electronic states of strongly correlated materials	Spatial resolution of several tens of nanometres and electric field sensitivity up to $2\,\mu V\,Hz^{-1/2}$	Only works under low temperature; spatial resolution is limited by the size of the device	[81]
Scanning capacitance microscopy	Capacitance	Dielectric and electrical properties of semiconductors and buried two-dimensional electron gas	Spatial resolution of several nanometres with capacitance sensitivity of attofarad	Spatial resolution is limited by the long-range capacitance coupling	[80]
Kelvin probe force microscopy	Contact potential difference	Local work function and electric dipole distribution of various samples	Nanoscale spatial resolution with sensitivity up to a single charge	Unsuitable for characterization of voltage-sensitive samples; spatial resolution is limited by the long-range electrostatic force	[82]
Piezoresponse force microscopy	Piezoelectric response of the sample	Ferroelectric ordering, piezo coefficient and energy dissipation	Spatial resolution with several nanometres	Tip wear can modify the tip–surface interaction, affecting imaging contrast; the acquired force signals may not always arise from piezo/ferro electricity phenomena	[83,84]

for investigating the local distribution of potential and inhomogeneous conductivity of metals and semiconductors[95]. Without the need for detecting the tunnelling current, scanning gate microscopy uses a conductive tip as the movable electric gate and is capable of revealing the local gating effects on the transport currents from the source and drain[96,97]. As the electrodes for transport measurements are usually fixed by nanofabrication, much more precise and flexible positioning of such electrodes was realized by multi-probe STM[98,99] (TABLE 5).

Near-field SPM. To optically probe the structural, dielectric and chemical properties with visible sub-wavelength resolution, scanning near-field optical microscopy (SNOM) was developed and has been widely used in the past decades[100] (TABLE 6). SNOM makes use of the evanescent components of the light highly confined near the surface, thus overcoming the diffraction limit of far-field optics. Generally, a sharpened optical fibre with a metal shield and a nanoscale aperture is used as the light source or detector for scanning. However, the spatial resolution is limited by the aperture size of the optical fibre, with a typical value of 30–50 nm. By contrast, apertureless SNOM such as scattering-type SNOM[101] uses a metallic AFM tip as the near-field scatterer and works in a dynamical mode for suppressing the background far-field signals, which improves the spatial resolution up to 1 nm (REF.[102]). Furthermore, making use of a sharp noble tip and highly confined surface plasmon[101], the efficiency of Raman scattering in the tip–sample gap is enhanced several orders of magnitude as compared with conventional far-field Raman experiments, such as

tip-enhanced Raman spectroscopy (TERS)[9,48]. Recently, TERS has demonstrated its ability in identifying and resolving chemical structures of single molecules with sub-nanometre resolution[9]. Benefiting from the local plasmon confined within the tunnelling junction, scanning tunnelling microscope-induced luminescence was also developed and applied for detecting the optical emission from the electronic and vibrational transition at the single-molecule level[103]. Apart from working within the range of visible light, it is also attractive for investigating the dielectric response of materials in the megahertz to gigahertz regime, such as microwave impedance microscopy, where a sharp metallic tip extended from a high-frequency resonator was used as the antenna to emit and collect microwave photons[104,105]. In contrast to conventional near-field SPM, photo-induced force microscopy[106] directly detects the near-field signal based on photo-induced dipolar forces, which efficiently suppress the overwhelming background signals.

Results

SPM images are always acquired as a 2D matrix, whereas spectroscopic curves are saved in the form of arrays. The main steps for data analysis include image inspection, noise analysis, filtering and image reconstruction. For the curves of SPM spectra and the line profiles of topographic images, a fitting procedure is usually necessary for interpretation of the underlying quantities and parameters. In this section, we showcase several representative examples to discuss how to analyse SPM images and spectra. The popular software for processing the SPM data are briefly introduced.

Scanning gate microscopy
A kind of scanning probe microscopy capable of probing electrical transport at the nanoscale, where a conductive tip is used as the local gate capacitively coupled to the sample.

Representative results

SPM imaging provides pseudo-3D data. As a surface probing technique, it does not deliver information about the inside volume of the object under investigation but provides an x–y grid of data points to each of which a single z height is associated. SPM data are thus most often represented as an x–y 2D image, where a false-colour scale represents the z height[107] (FIG. 5a). Sometimes, SPM data are represented as a 3D surface shown in perspective (FIG. 5b) that is visually attractive but scientifically less precise because at least one of the in-plane axes is skewed, the z height sometimes increased and some structural features obstructed by the perspective view. In the SPM field, unfortunately, no stringent standards have been established regarding the representation of SPM data in publications, and sometimes filters are used to display images. Specifically, the application of short-range median filters in the y dimension, which cancel lines from the fast scan axis (x dimension) of the image acquisition, is common.

Force–distance curves are acquired by recording the deflection signal of the AFM cantilever while controlling the tip–sample distance. For example, when the tip approaches the surface and interacts with the biomolecules, the interaction force is detected and used to describe the deformations of the sample[33] (FIG. 5c). On the other hand, upon withdrawing the tip, the force–distance curve can be used to infer multi-mechanical parameters such as adhesion, Young's modulus, plastic deformation and energy dissipation of the sample through fittings.

STS is suitable for investigating the local density of states of a sample. In FIG. 5d, a typical dI/dV curve acquired on a single pentacene molecule shows prominent peaks at both the positive and negative biases, which are attributed to the highest and lowest molecular orbitals (HOMO and LUMO, respectively)[37]. By fixing the bias at the LUMO or HOMO and spatially mapping out the dI/dV intensity, the frontier orbitals of the single pentacene molecule can be directly visualized in real space[37] (FIG. 5f). Whereas the STM mode is only sensitive to the electronic states near the Fermi level, non-contact AFM working under the frequency modulation mode is able to probe the total electron density of the sample by entering into the region of short-range Pauli repulsion[108]. In FIG. 5g, a CO-functionalized tip clearly resolves the chemical skeleton of the single pentacene molecule, where the short-range Pauli repulsion dominates the

Table 4 | **Liquid-phase scanning probe microscopy techniques**

Name	Detected signal	Utility	Resolution	Disadvantages and limitations	Refs
Scanning ion conductance microscopy	Ion current	Non-invasive imaging of the tomography and investigation of the physiological properties of complex biological systems such as living cells in solutions	Spatial resolution with several tens of nanometres	Spatial resolution is limited by the size of the microchannel	91,92
Fluidic force microscope	Deflection of the cantilever	Single-cell manipulation and controlled delivery of bioactive agents	Sub-micrometre	Spatial resolution is limited by the size of the microchannel	93,94
Liquid-phase scanning tunnelling microscope	Tunnelling current	Investigation of supramolecular systems and their self-assembly, dynamics and reactivity	Atomic resolution	Tip condition is not well controllable compared with scanning tunnelling microscopy in an ultra-high vacuum; only a conductive surface could be investigated	85–87
Electrochemical scanning tunnelling microscopy	Tunnelling current	In situ detection of various electrochemical processes, such as formation of an electrochemical double layer, metal corrosion and electrodeposition	Atomic resolution	Tip condition is not easily controllable for electrochemical reactions; Faraday currents interfere with the tunnelling current	17,88
Liquid-phase non-contact atomic force microscopy	Frequency shift	In situ detection of the structure of the hydration layer and electrochemical double layer on a solid–liquid interface with atomic resolution	Atomic resolution	Three-dimensional force mapping for structural analyses on solid–liquid interfaces is time consuming; only local liquid density can be probed	89,90

Table 5 | **Transport-compatible scanning probe microscopy techniques**

Name	Detected signal	Utility	Resolution	Disadvantages and limitations	Refs
Scanning tunnelling potentiometry	Tunnelling current	Imaging of the spatial distribution of electrostatic potential	Atomic resolution in principle	Interpretation of the signal is difficult because distinguishing tomography from potentiometry is challenging	[95]
Scanning gate microscopy	Conductance between source and drain electrodes	Spatial mapping of electron flows in two-dimensional materials and semiconducting materials	Spatial resolution of several tens of nanometres	As the capacitive coupling between tip and sample is long range, the spatial resolution is largely limited by the sharpness of the tip apex and the tip–sample distance	[96,97]
Four-probe scanning tunnelling microscopy	Tunnelling current	Local and in situ investigation of in-plane electronic transport properties	Atomic resolution in principle	Closest distance (10–20 nm) between the probes is limited by the curvature radius of the tip apex; performance is generally poorer than that of conventional scanning tunnelling microscopy owing to the complex scanner design	[98,99]

tip–molecular interaction[108]. The sharp lines arise from the electron density build-up across the covalent bonds between the carbon atoms.

In some cases, inelastic electron tunnelling signals may be superimposed on the large background of elastic tunnelling conductance during STS measurements. For example, the dI/dV curve taken on the bilayer NaCl(001) film grown on Au(111) demonstrates a broad peak (grey), which corresponds to the interfacial electronic states[109] (FIG. 5e). When the tip is positioned on the water molecule adsorbed on the surface, distinct kinks appear in addition to the interfacial electronic states (red). Such kinks are more clearly resolved as dips and peaks in d^2I/dV^2 spectra, which are point-symmetrical with respect to the zero bias. The energy positions of those features reflect the energies of different vibrational modes of the single water molecule.

Visualization and analysis software
The major problem of image visualization and image analysis originates from the fact that, so far, no common SPM file format has been established. Each SPM company has a specific proprietary file format and microscope-associated software for image data analysis. Among others, Gwyddion[110], WSxM[111] and ImageJ are free and open source software. They are likely the most powerful SPM data visualization and analysis platforms, as they provide a large number of data processing functions. These include standard statistical characterization, data correction, filtering and grain marking functions. Gwyddion and WSxM are compatible with most standard file formats (such as .dat, .txt and .sxm) acquired from commercial SPM programs such as Nanonis, Omicron and RHK. ImageJ has the advantage that it is widely used by the optical fluorescence microscopy community and, thus, features a large variety of functions that can be adapted for SPM data, and its capabilities are rapidly growing through contributions of analysis tools from a large scientific community.

Here, we take the application of AFM in biology as an example. When AFM is used for cellular imaging, either proprietary software is used for analysis or images are exported in various file formats such as .tiff, .raw, .png, .sxm and .gwy to be analysed by laboratory-written routines in the software packages mentioned above or in MATLAB[112]. Analysis of data from the above-described hybrid imaging/nanomechanical mapping modes[113] is often done in proprietary application mode software; in this case, not only the data encoding but also the acquisition process is system-dependent. When AFM is used for molecular imaging and analysis of protein structures and conformations, AFM users often borrow methods from electron microscopy. The recent progress in electron microscopy to solve protein structures[114] is directly associated with image analysis developments. To this end, there is a plethora of such programs for analysis of macromolecular structures, such as EMAN[115], IMAGIC[116], SPIDER[117] and RELION[118]. Given that the contrast transfer function and the noise distribution of AFM are very different from those of electron microscopy, these programs must be adapted with care. SEMPER and MRC are most powerful to analyse 2D crystalline data[58], and most other programs are adapted to analyse single particles[119].

Analysis of biological data
When using AFM for the analysis of images of proteins, one particle is used for a cross-correlation search of all other molecules in the image. Next, cross-correlation-based lateral and rotational alignment of the particles is performed. Particle selection based on cross-correlation values can be performed to calculate an average of the most common particle structure[120]. During the averaging process, a standard deviation map can be calculated that highlights the most flexible parts in the molecule[121]. From the stack of particle images that one has extracted using cross-correlation searches, one can statistically assess any parameter of

interest characterizing the molecule, such as the height and volume distribution of the particles[122], or molecular symmetry[123]. For example, the complete perforin 2 rings shown in FIG. 5a can be distinguished from incomplete arcs using cross-correlation-based selection and laterally and rotationally aligned to calculate an ensemble average (FIG. 5a, insets). For the analysis of filamentous structures, such as DNA or filamentous proteins, automated particle detection based on the height above the background, followed by tracing of the filaments, allows direct extraction of the physical properties of the filament, such as its persistence length[124]. Unfortunately, structural analysis using automated programs is not utilized enough in the AFM field, and it is still rather common to place arrows on image panels to highlight features instead of calculating relevant molecular

representations accompanied with statistical data, as is done in the electron microscopy field.

Applications

SPM has found a multitude of applications in the natural sciences. In the following, we divide those applications into physics, chemistry, materials science and biology, although they are often closely linked to each other and have strong overlap.

Examples from physics
Surface science. The initial application for STM was in the field of surface science, where atomic-scale arrangement as well as the electronic properties of materials needed investigation. The key initial experimental evidence for the power of STM in this regard was the

Table 6 | **Near-field scanning probe microscopy**

Name	Detected signal	Utility	Resolution and sensitivity	Disadvantages and limitations	Refs
Scanning near-field optical microscopy	Emission of fluorescence or adsorption of excitation lights	Local fluorescence imaging of biological molecules and photoluminescent spectroscopy of semiconductors	Spatial resolution with tens of nanometres	Spatial resolution is largely limited by the size of the nanofibres used as probes; near-field signal is weak and easily disturbed by metallic coatings	100
Scattering-type scanning near-field optical microscopy	Elastic scattering of lights	Local dielectric response from optical light and plasmonic structures	Spatial resolution up to 1 nm and monolayer sensitivity	Requires cantilevers to work under large amplitude to eliminate far-field background, making the method insensitive to short-range tip–sample interactions	101,102
Tip-enhanced Raman scattering	Raman scattering of lights	Analysis and identification of the local chemical structure of small molecules, biomolecules, living cells and two-dimensional materials	Single-molecule sensitivity and sub-nanometre spatial resolution	High spatial resolution relies on the electromagnetic coupling between the tip and a plasmonic substrate, thus limiting the systems that can be studied	9,48
Scanning tunnelling microscope-induced luminescence	Photon emission from sample	Photon yield images and energy-resolved spectroscopic images	Single-molecule sensitivity and sub-nanometre spatial resolution	High spatial resolution relies on the electromagnetic coupling between the tip and a plasmonic substrate, thus limiting the systems that can be studied	103
Microwave impedance microscopy	Reflection or transmission parameters of microwaves	Local dielectric properties and conductivities; suitable for obtaining information from a buried interface	Spatial resolution of several tens of nanometres	Spatial resolution is limited by the long wavelength of microwave photons	104,105
Photo-induced force microscopy	Photo-induced dipolar interactions	Detection of both topography and chemical signature on organic and inorganic samples	Spatial resolution of sub-10 nm and monolayer sensitivity	Quantitative interpretation of the imaging contrast is difficult; only works with the narrow band of infrared lights	106

atomic-scale imaging of the Si(111) 7×7 reconstructed surface[125]. Here, STM was able to offer insight that was hard to gain from reciprocal space tools such as low-energy electron deflection (LEED). In particular, the surface reconstruction containing multiple atoms within a unit cell yields a very complicated diffraction pattern when using LEED, from which it is difficult to deduce the exact atomic arrangement. In other words, different atomic-scale models could give rise to the same LEED pattern. By contrast, STM directly images atoms in real space and eliminates the uncertainties of structural determination through model building.

Atomic defects. In contrast to reciprocal space tools such as LEED, STM is able to measure individual defects in materials, one at a time. This is beautifully exemplified

by the imaging of dopant atoms in semiconductors[126,127]. STM allows the imaging of embedded dopants for up to about ten atomic layers below the surface[128], showing an intricate shape that depends on the band structure of the material as well as the electron scattering properties of the defect[126,127]. Great care has to be taken with the interpretation of conductance spectra in these systems as the presence of the metallic tip over a semiconductor or thin insulator can dramatically change the electronic band structure, an effect referred to as tip-induced band bending[129]. When combined with femtosecond or nano-second laser pulses, ultra-fast charge dynamics of defects can be mapped out in real space at nanoscales[63,130].

Scanning probes can also modify materials on the atomic scale. In semiconductors, STM can be used to desorb individual hydrogen atoms from a
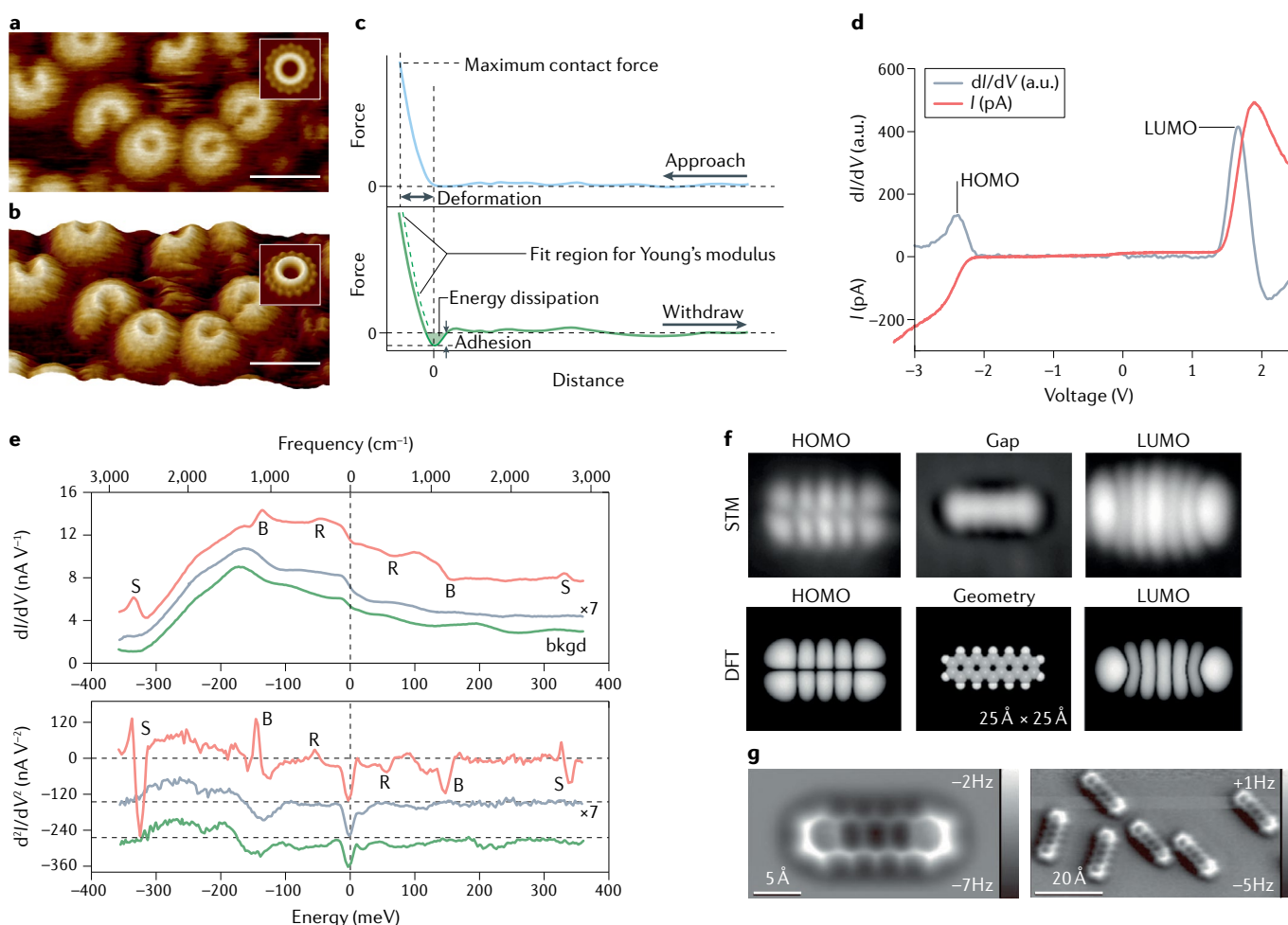

Fig. 5 | **Typical results of scanning probe microscopy experiments.**
a | Visualization of atomic force microscopy (AFM) data. A high-speed AFM image of perforin 2 (PFN2) prepore rings and arcs recorded in physiological buffer and at room temperature (full false colour scale: 8.5 nm). Scale bar: 20 nm. b | Pseudo three-dimensional (3D) representation of the high-speed AFM image. Insets: correlation average of 16-meric PFN2 prepore ring. Scale bar: 20 nm. c | Force–distance curve showing different mechanical properties of the surface. d | I/V (red) and dI/dV (blue) curves demonstrating the highest and lowest molecular orbitals (HOMO and LUMO) of a single pentacene molecule. e | Scanning tunnelling spectroscopy (STS) spectra acquired using a chlorine tip, showing the interfacial electronic states of sodium chloride and gold(111) (green spectra) and the vibration modes

of adsorbed water molecules (red spectra, tip height −1.2 Å; grey spectra, tip height −0.4 Å). f | STS image acquired by a pentacene tip showing the frontier orbitals of single pentacene, which is in good consistence with density functional theory (DFT) simulation. g | AFM image with a CO tip clearly visualizing the skeleton of a single pentacene molecule. STM, scanning tunnelling microscopy. B, bending mode; R, rotation mode; S, stretching mode. Part a adapted with permission from REF.[107], AAAS. Part b adapted with permission from REF.[107], AAAS. Part c adapted from REF.[33], Springer Nature Limited. Part d adapted with permission from REF.[37], APS. Part e adapted with permission from REF.[109], AAAS. Part f adapted with permission from REF.[37], APS. Part g adapted with permission from REF.[108], AAAS.
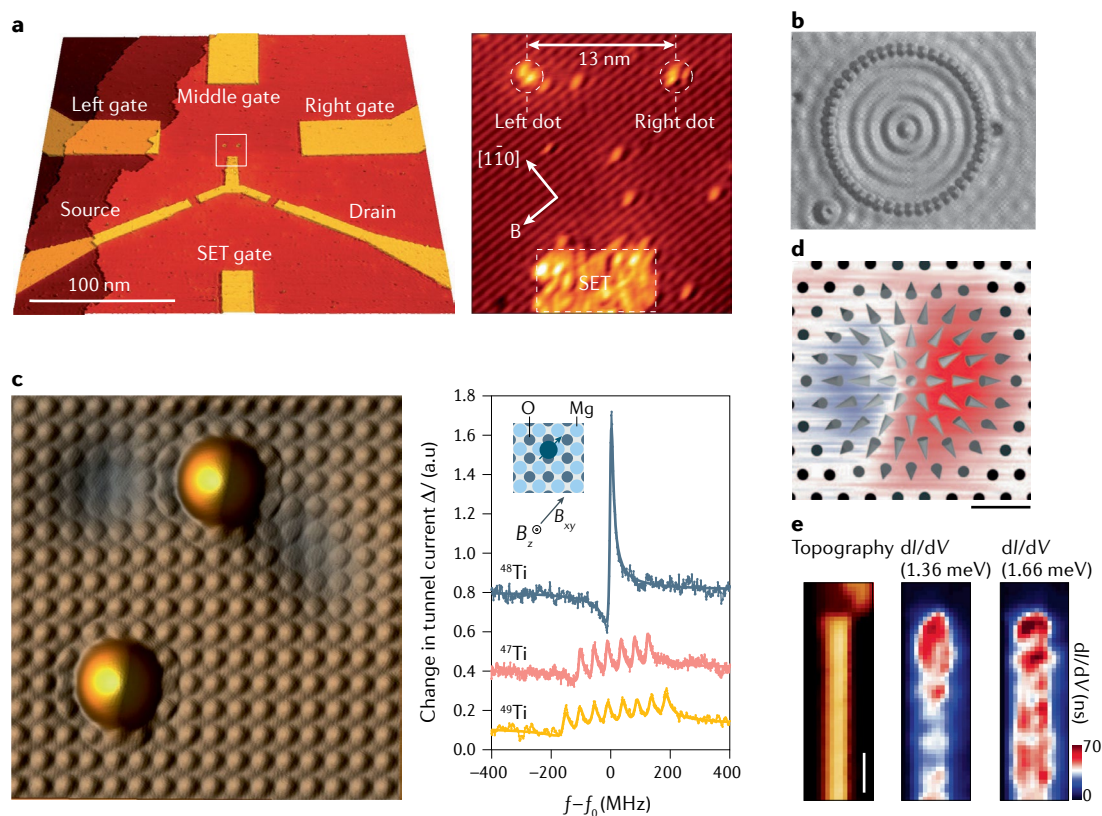
Fig. 6 | **Applications of scanning probe microscopy in physics. a** | Scanning tunnelling microscopy (STM) tomographic image of a two-qubit quantum device (left dot and right dot) fabricated through STM lithography with atomic precision inside silicon. Such a device includes four electric gates, which are used for tuning the electrochemical potential of these qubits and, thus, the speed of such an exchange gate. **b** | Quantum corral constructed by 48-atom iron on a Cu(111) surface. Average diameter of this corral is 142.6 Å, whereas its edge encloses a defect-free region of the surface. **c** | STM image with a hydrogen-terminated tip of two magnetic atoms on a magnesium oxide film on a silver substrate (4.5 nm)[2]. Electron spin resonance (ESR) STM spectrum measured on three different titanium atoms. Most titanium atoms show a single ESR line. Approximately 7% show six lines and 5% show eight lines. **d** | Single skyrmion measured by spin-polarized STM superimposed by the schematic spin configuration. The asymmetrical feature results from the canted tip's magnetization. Scale bar: 5 nm. **e** | Topographic image of the atomic chain (left) and spatially resolved dI/dV maps for $|eV_1| = \Delta_T = 1.36$ meV (middle) and $|eV_2| = \Delta_T + 0.3$ meV (right). Scale bar: 20 Å. Maximum on one end of the chain indicates the Majorana quasi-particle state. SET, single-electron transistor. Δ_T, superconducting gap of the tip; eV, electron volt. Part **a** adapted from REF.[132], Springer Nature Limited. Part **b** adapted with permission from REF.[10], AAAS. Part **c** adapted with permission from REF.[76], AAAS. Part **d** adapted with permission from REF.[135], AAAS. Part **e** adapted with permission from REF.[138], AAAS.

hydrogen-saturated silicon surface[131]. The resulting reactive dangling bonds can then be used to incorporate dopants at precisely defined positions. When such a sample is then overgrown with more silicon, it becomes possible to place dopants underneath a silicon surface with atomic-scale spatial precision. This, in turn, offers the possibility to use them as quantum bits for quantum information studies[132] (FIG. 6a).

Atoms on surfaces. Perhaps the prototypical application of STM and AFM in physics is the investigation of individual atoms on surfaces of various materials. The equally important area of molecules on surfaces will be discussed below. If atoms are deposited onto cold (<20 K) metal surfaces, such as Cu(111), then they will absorb in random positions. However, atoms can be moved with atomic-scale precision to any desired binding site[11]. This approach was used to build quantum corrals[10] (FIG. 6b),

computing devices with molecule cascades[133] and artificial quantum materials[134]. AFM has been used to measure the atomic forces involved in these manipulations[45], and AFM at UHV and low temperature now has better spatial resolution than STM by probing the short-range forces with functionalized tips[108]. The combination of AFM (which is sensitive to the atomic configuration) with STM (which is sensitive to the electronic structure) can combine electronic, magnetic and structural information in a single measurement tool — often enabled through the qPlus sensor[28].

Spins on surfaces. Magnetic atoms on surfaces were first investigated in thin films[71] where STM and AFM can be converted into spin-polarized variants, which are sensitive to the magnetic orientation of the atoms. Because of the real-space power of these techniques, intriguing spin textures such as spin spirals and skyrmions were

imaged and manipulated[135] (FIG. 6d). Interestingly, when single atoms retain a spin character on a metal surface, they enter a strongly correlated electronic state with the underlying conduction electrons, called a Kondo effect[136], with a typical interaction energy of tens of millielectron-volts. This interaction can be weakened dramatically by replacing the normal metal with a superconductor. The magnetic interaction can then be observed as Yu–Shiba–Rusinov excitations within the band gap of the superconductor (less than 1 meV)[137]. This was extended to spin chains on non-trivial superconductors, in search of the elusive Majorana mode, which is supposed to localize at the ends of chains[138] (FIG. 6e).

The spin character of magnetic atoms[38] or chains of atoms[139] can be preserved when decoupling the spins from a metal by a thin insulating film. This allowed a development of fast STM by means of all-electrical pump-probe spectroscopy[62] with a time resolution of 1 ns, to probe the spin dynamics of single atoms. There is a strong urge to utilize quantum-coherent functionality in nanoscale structures, materials and devices. STM has only recently entered the field of coherent manipulation of spins by combining the high spatial resolution of STM with the high energy resolution of ESR[75]. Such a system needs to incorporate gigahertz microwave excitations into low-temperature STM. In practice, the DC bias voltage of STM is preplaced by a gigahertz-frequency AC field possibly added on top of a DC voltage. This high-frequency voltage converts to an oscillating electric field in the tunnel junction, where it can drive coherent spin manipulation. FIGURE 6c shows an example of the applications of ESR-STM to probe the spin of titanium atoms (with an attached hydrogen) on magnesium oxide, where most atoms show a single ESR line, whereas some show six lines and others eight lines. The different spin energy structures between those titanium hydride atoms stem from a different nuclear isotope that has a strong hyperfine interaction with the electron spin[76].

Examples from chemistry
Single-molecule chemistry. The birth of SPM has opened up a fascinating opportunity of probing and controlling chemistry at the single-molecule level[43,140]. The frontier orbitals of molecules play an important role in chemical reactions, and can be selectively imaged at the sub-molecular level by the tunnelling electrons of STM[37,56]. Remarkably, orbital imaging has been applied to capture the proton-transfer reaction in real time, even if the reaction-induced change in the STM image is very subtle[141]. In addition to real-space imaging, vibrational spectroscopy based on STM-IETS was successful for the chemical identification of different isotopes[142,143] (FIG. 7D), quantitative determination of the intermolecular interaction[109] and exploring the fundamental effects of molecular vibration on surface chemical reactions[144]. The tunnelling electrons of STM are not only probes but also act as powerful handles for triggering chemical reactions (FIG. 7A), such as selective bond formation/breaking[42,44,140], diffusion/desorption[145,146] and reduction/oxidation[147], through vibrational and electronic excitation. STM has become a routine tool to identify the active sites on metallic[148] or semiconducting[149,150]

catalytic materials, which is vital for unveiling the underlying mechanism in surface catalysis. Ultra-fast dynamics such as coherent molecular vibrations could be approached by incorporating terahertz[66] or femtosecond[151] optical pulses in STM systems.

As STM is only sensitive to frontier molecular orbitals near the Fermi level, resolving atoms within the molecules is not so straightforward. Thanks to the high sensitivity of qPlus-based non-contact AFM to the atom position by probing the short-range Pauli repulsion forces[108] and high-order electrostatic forces[54], the chemical structure and chemical bonds of a single molecule can be directly visualized in real space with a CO-functionalized tip (FIG. 7C). This technique allows the identification of both the metastable states and the by-products along the reaction coordinates[152]. When combined with STM, non-contact AFM provides an unprecedented chance for identification and control of multiple charge states of single molecules on insulating films[153,154], which are key steps during chemical reactions. Furthermore, the force versus distance curves contain characteristic fingerprints arising from the complex interplay between the van der Waals, electrostatic, chemical and repulsive forces, which can be further harnessed for elemental recognition[155] and structure analysis[108]. STM, non-contact AFM and TERS have been combined to achieve the univocal characterization of the structural and chemical heterogeneities of single molecules with single-bond resolution[156].

Chemical reaction at liquid–solid interfaces. Many heterogeneous chemical reactions occur at liquid–solid interfaces, which are quite different from the vacuum condition or gas phase for single-molecule chemistry as described in the previous section. Molecular and nanoscale information of various electrochemical processes such as the formation of an electrochemical double layer[157], metal corrosion[158] and electrodeposition[159] can be obtained by EC-STM at solid–electrolyte interfaces. Recently, the catalytically active sites at solid–electrolyte interfaces have been successfully identified by monitoring the noise of the tunnelling current[17]. In addition, EC-STM also allows imaging of the structural phase transition induced by electrode potential or redox-induced charge state variation[160]. Characterizing liquid–solid interfaces is ideal with non-contact AFM, as it removes the need for imaging on conductive substrates. Both soft cantilever-based[89,161] and qPlus-based[162,163] systems work well in aqueous conditions to achieve atomic resolution. Various substrates ranging from inorganic crystals[164] to interfacial organic molecules[165,166] were extensively investigated by non-contact AFM in solutions. Furthermore, non-contact AFM can also probe the atomic-scale interaction between substrates and solvent/solute molecules by mapping the tip–surface force in a 3D manner[90,165,166]. Using such a technique, the 3D periodicity of hydration layers on mica[90,167] and the specific atomic-scale patterns on calcite substrates[168] were visualized. Exotic laser-combined SPM techniques also provide new insights into the field of chemistry at solid–liquid interfaces. For example, by applying a sharp plasmonic tip and the TERS technique, redox reaction

processes[49] and catalytical sites[169] have been visualized with nanoscale resolution.

Chemistry at liquid–solid interfaces can also be investigated ex situ under UHV conditions. In such experiments, the solid substrates are immersed in solution or topped by a droplet outside the UHV chamber[170–172]. The interfacial solution layer may survive after transferring the sample to the vacuum environment, allowing for high-resolution SPM characterization. To avoid unwanted contaminants in the air, preparation of the ultra-pure water droplet on solid surfaces can be done directly inside the UHV chamber[173]. Using this method, hydration structures on various metal oxide surfaces could be investigated with atomic resolution[174]. For the chemical reactions at liquid–solid interfaces, the structure and dynamics of hydrates play an important role, but have been poorly understood until very recently. SPM has been used to construct individual sodium hydrates at a salt surface containing different quantities of water

molecules[175], which revealed correlation between ion transport and hydration numbers (FIG. 7E).

Molecular self-assembly on surfaces. On-surface synthesis of molecular networks and nanoarchitectonics based on surface self-assembly has received increasing attention in the past few decades[176]. The detailed topology of the molecular networks can be distinguished by high-resolution SPM. For example, high-quality imaging at the solid–liquid interface between non-ionic organic liquids and atomically flat conductive substrates has been achieved by both STM[85–87] and AFM[177,178]. Also, intermolecular interactions have been extensively investigated by STM in both vacuum–solid[179,180] and liquid–solid[181] interfaces. In particular, the covalent-bonding[180,182], coordinate-bonding[183], hydrogen-bonding[184,185] and halogen-bonding[186,187] structures of molecular assemblies were resolved at the single-bond level. In addition to imaging, the SPM tip can be used to construct
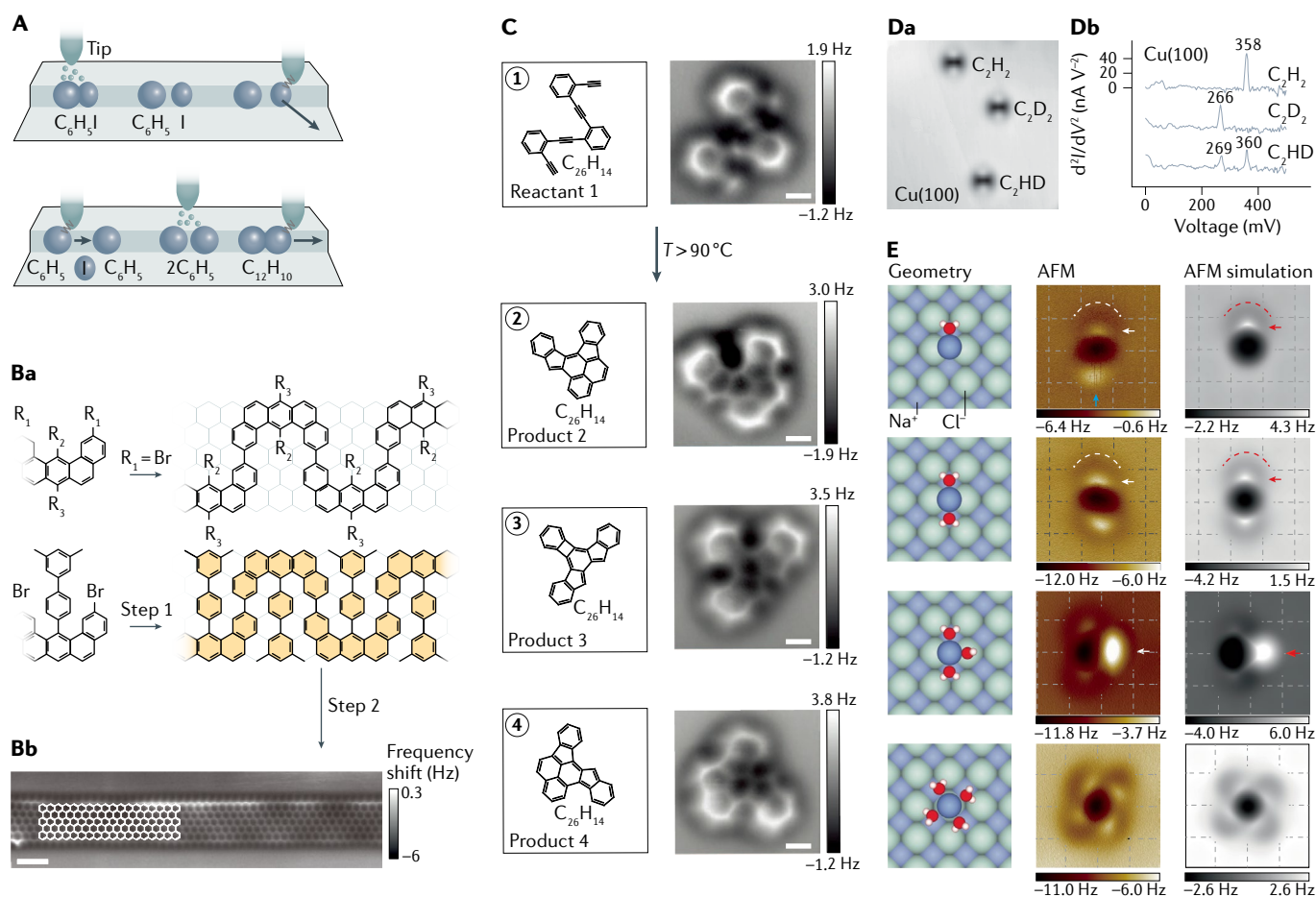

Fig. 7 | **Applications of scanning probe microscopy in chemistry.** **A** | Schematic of the scanning tunnelling microscopy (STM) tip-induced synthesis steps of a biphenyl molecule. **B** | Models showing procedures of the precursor molecules (part **a**) and constant-height non-contact atomic force microscopy (AFM) image of the synthesized graphene nanoribbons (part **b**). **C** | Non-contact AFM image of the reactant molecule (1) and its corresponding products (2, 3 and 4) acquired by a CO-modified tip. **D** | STM image (part **a**) and single-molecule vibrational spectra (part **b**) of three acetylene isotopes on Cu(100) at 8 K demonstrating isotope identification through distinct stretching-mode energy. **E** | Geometries and high-resolution AFM images of sodium hydrates. Atomic models (first column shows top view), AFM images (acquired with a CO tip) and AFM simulations of Na⁺·nD₂O clusters (n = 1–4) demonstrated. Hydrogen, oxygen, chlorine and sodium atoms are denoted as white, red, green and purple spheres, respectively. Square lattices of the NaCl(001) surface arising from Cl⁻ are depicted in the AFM/simulation images by dashed grids. Part **A** adapted with permission from REF.[140], APS. Part **B** adapted from REF.[182], Springer Nature Limited. Part **C** adapted with permission from REF.[152], AAAS. Part **D** adapted with permission from REF.[143], APS. Part **E** adapted from REF.[175], Springer Nature Limited.
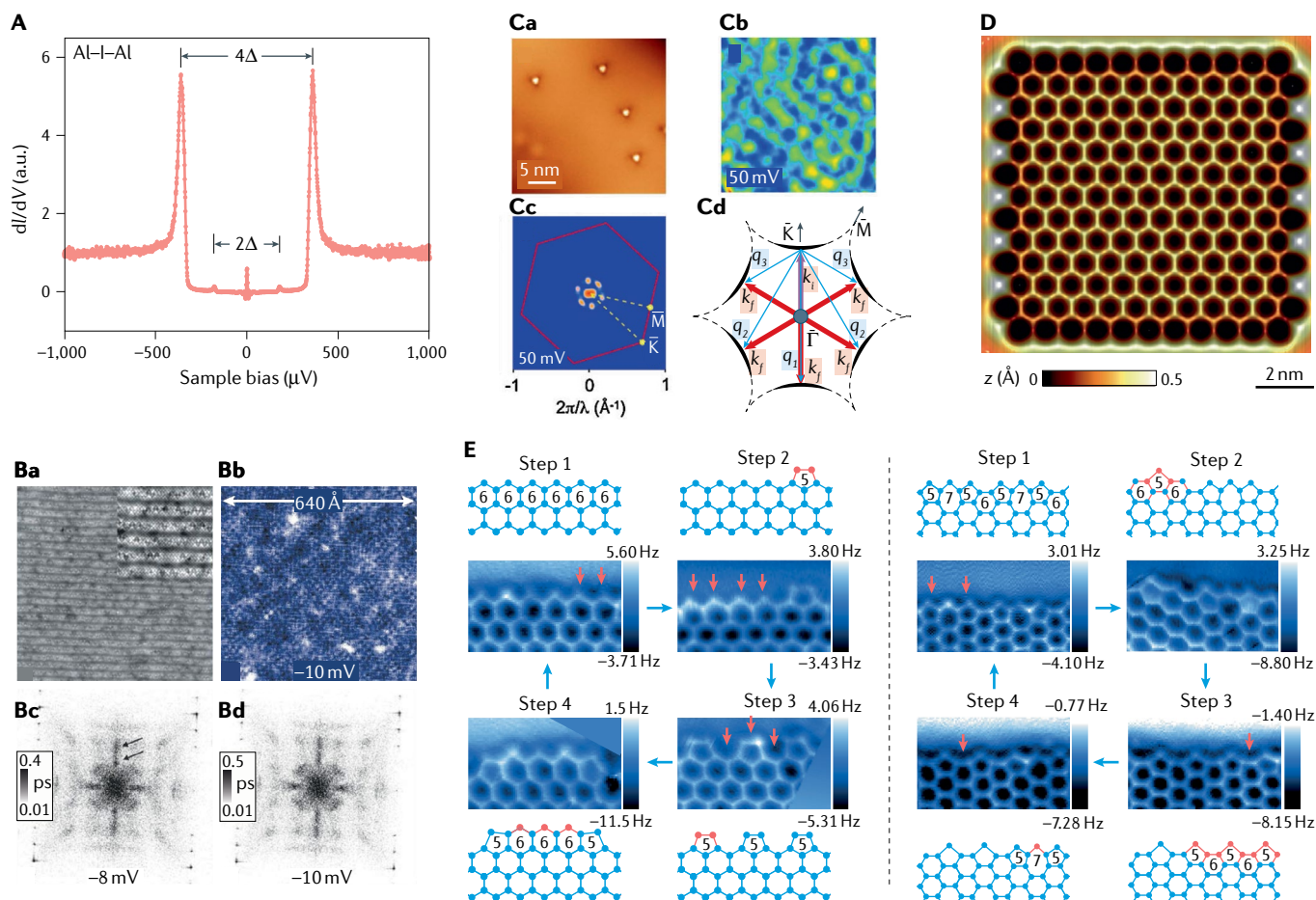
Fig. 8 | **Applications of scanning probe microscopy in materials science. A** | d*I*/d*V* spectra of a superconducting Al(100) sample with an aluminium tip. **B** | Atomic resolution of the bismuth oxide surface (part **a**), d*I*/d*V* mapping of the same region at −10 mV (part **b**) and fast Fourier transforms of a typical quasiparticle interference (QPI) pattern at different energies of d*I*/d*V* mapping (parts **c,d**). Non-dispersive signals marked by arrows. **C** | Scanning tunnelling microscopy (STM) image showing silver trimers on bismuth telluride(111) (part **a**), d*I*/d*V* mapping at specific energies showing the standing waves (part **b**), scattering geometry showing all possible scattering vectors ($\vec{q}_1$, $\vec{q}_2$, $\vec{q}_3$) between states on the same energy constant ($\vec{k}_i$ and $\vec{k}_j$) (part **c**) and absent components of $\vec{q}_1$ and $\vec{q}_3$ in in the QPI indicating supressed backscattering of this topological surface state (part **d**). **D** | STM image of a molecular graphene lattice constructed by 149 CO molecules. Lattice constant is 8.8 Å. **E** | High-resolution non-contact atomic force microscopy (AFM) images showing the growth process of two-dimensional (2D) ice. Both zigzag and armchair edges are monitored step by step. Scanning area: 3.2 nm × 1.9 nm. Part **A** adapted with permission from REF.[22], AIP. Part **B** adapted from REF.[198], Springer Nature Limited. Part **C** adapted with permission from REF.[208], APS. Part **D** adapted from REF.[218], Springer Nature Limited. Part **E** adapted from REF.[184], Springer Nature Limited.

or modify the supramolecular phase through precise manipulation[42,140], ranging from synthesizing individual molecular units[140] to establishing 1D (REF.[188]) or even 2D (REF.[189]) molecular networks.

One representative application of on-surface assembly based on covalent coupling is the synthesis and engineering of graphene nanoribbons with atomic precision in a bottom-up manner[182,190] (FIG. 7B). The precise control of the width and edge structure of graphene nanoribbons was achieved by depositing appropriate precursors, followed by the on-surface reactions finely tuned through the annealing temperature. Notably, the intermediate polymer structures and the final products with a flatter geometry after cyclodehydrogenation were identified by AFM. In addition to obtaining the geometric structure, STS measurements also yield valuable information on the electronic structure of graphene nanoribbon-based

heterojunction[191], spin polarization[192] and the topological properties[193,194] of edge states.

Examples from materials science

Superconductors. STM is an ideal tool for exploring the microscopic origin of superconductivity, owing to its ability to probe the electronic and vibrational states at the atomic scale both in real and momentum space. Indeed, STM-IETS was used to unveil the correlations between electronic properties and lattice vibrations of superconductors in real space[195]. The energy resolution of STM can be greatly enhanced (up to 10 µeV) by using a superconducting tip, which allows precise determination of the superconducting gap arising from the formation of Cooper pairs in d*I*/d*V* spectra[22] (FIG. 8A). Meanwhile, through mapping the d*I*/d*V* signals under zero-bias voltage, the local magnetic vortices, which are

---

Cooper pairs
Pairs of electrons bound together through electron–phonon couplings, which are responsible for explaining superconductivity.

Quasiparticle interference
(QPI). Interference caused by the coherence of quasiparticles, inherently a kind of collective disturbance that behaves as a single particle.

QPI imaging
Imaging showing the quasiparticle interference (QPI).

the characteristic features of type II superconductors in a magnetic field, were directly visualized[196]. Spectroscopic mapping at different bias voltages is also a powerful tool for obtaining the momentum-space information based on quasiparticle interference (QPI), where the wavevectors of resulting standing waves can be obtained by Fourier transformation of dI/dV images[197,198] (FIG. 8B). QPI imaging allows extraction of intriguing electronic properties such as band structure[197,198], non-dispersive periodic electronic modulation[199] and pairing symmetry[200]. Particularly, it is possible to visualize the local charge ordering in superconducting[201], pseudogap[199] and Mott states[202]. Both cuprate-based[201] and iron-based[200,203] high-temperature superconductors have been extensively investigated with this method, where the spatial correlation between charge and/or magnetic order and superconductivity was revealed. The proposed underlying mechanisms include the stripe order[204], Fermi surface nesting[205], Fermi arc instability[206] and Cooper pair density wave[207].

Topological materials. Topological insulators are insulating in the bulk while processing metallic states on the surface, which are called topological surface states. Such gapless states connecting the bulk band gap are topologically protected and robust against external disturbances[208], leading to great potential in various applications such as non-dissipative electronics. As a surface-sensitive electronic probe, STM is suitable for investigating topological surface states and its response to local atomic-size impurities. Both the discrete Landau levels of topological surface states under a magnetic field[209] and the band structure evolution along with electric gating can be resolved by STS measurements[210]. The forbidden backscattering of the quasiparticles, which is a key feature of topological surface states, was confirmed through analysis of the QPI patterns around individual non-magnetic scattering centres such as adsorbed atoms[208] or defects[211] (FIG. 8C). The influence of charged and magnetic impurities on electron mobility has also been investigated[212]. So far, STM has shown unique ability to provide atomic-scale insights into various quantum materials with topological protection, such as topological superconductors[213], topological crystalline insulators[214], topological semimetals[215] and Majorana fermions[138,216,217]. Based on the advanced molecular manipulation techniques of STM, scientists are able to build artificial 2D topological materials from CO molecules[218,219] (FIG. 8D) or create vacancies in chlorine monolayers[220], which provide new possibilities for engineering topological states and exploring new exotic quantum phases.

Two-dimensional materials. The electronic, optical and magnetic properties of atomically thin 2D materials are extremely susceptible to local corrugations, ripples, boundaries and reconstructions, which can be perfectly probed by STM and AFM with atomic resolution[221,222]. Characteristic electronic properties of graphene such as Dirac points[221], phonon-assisted tunnelling[221], electronic chirality[223], pseudospin[223] and inter/intra-valley scattering[224] have been revealed by

STM and QPI measurements. It is also possible to probe the edge states and local band structure of both single-layer[225] and bilayer[226] heterojunctions or the heterophase[227,228] of transition metal dichalcogenides. More recently, increasing efforts have been made to locally probe strongly correlated quantum phenomena such as superconducting phases[229] and cascade phase transition[230,231] on twisted bilayer 2D materials using exotic SPM techniques such as scanning SQUID and scanning single-electron transistor microscopy. Another unique application of SPM is using a conductive tip for local electric gating to achieve charge state control of single defects[232] and local tip-induced phase transitions[233].

In order to probe the optical properties of 2D materials at the nanoscale, scattering-type SNOM has been used because of its high spatial resolution beyond the optical diffraction limit[102], where the metallic tip eliminates the momentum mismatch between the free space photon and confined surface plasmon polaritons[234]. Hence, it is possible to probe both the local properties and the propagating behaviour of surface plasmon polaritons in 2D materials by analysing the interference patterns in real space[235]. SPM is also ideal for probing magnetism and ferroelectricity of 2D materials. For example, the atomic magnetic structure of 2D ferromagnetic materials such as chromium bromide has been unveiled by spin-polarized STM[236], which clarified the relation between the stacking order and magnetism. In addition, local electric and structural analyses of 2D ferroelectric materials have also been correlated by AFM and PFM[237].

In addition to the static properties, the real-time monitoring of the growing process of graphene on nickel substrates has been achieved using video-rate STM[15], which captured the catalytic action of a single adjacent nickel atom at the edges of growing graphene flakes. Very recently, the CO tip of qPlus-AFM was used to resolve highly fragile edge structures of 2D ice, thanks to the weakly perturbative nature of the tip[184]. Notably, various metastable and/or intermediate edge structures involved in ice growth were frozen and imaged, allowing reconstruction of the ice growth process (FIG. 8E).

Functional materials. To date, SPM has been successfully used to image the surface of photovoltaic and optoelectronic materials, such as the perovskite-based materials. For example, STM and AFM has been applied to investigate halide perovskite[238,239] with atomic resolution. The alignment of organic and inorganic atoms in halide perovskites, as well as the domain structures[240], could be clearly resolved. SPM has also found wide applications in ion batteries, by quantitively characterizing the topographic, mechanical and electrochemical properties at the electrolyte–electrode interface with nanoscale resolution. One prominent example is the in situ AFM observation of the growth of the solid–electrolyte interface layer on the electrode in a lithium ion battery[241], which results from the decomposition of the electrolyte during an electrochemical process. In addition, the insertion/de-insertion of lithium ions during the charging and discharging processes can also be sensed by conductive AFM, owing to the changes in the electrical properties of

the electrode materials[242]. However, the spatial resolution in such materials is still far from the atomic scale.

Meanwhile, other kinds of functional materials such as multiferroic materials have also been extensively investigated through SPM. Multiferroic materials possess both ferroelectric and magnetic orders[243]. The spontaneous polarization and magnetization orderings of multiferroics either arise independently or appear under mutual induction through magnetoelectric couplings. A powerful method for multiferroic research is PFM, which can probe and manipulate multiple ferroelectric properties in real space with nanometre precision[83]. Both the relative polarization strength and the direction of static domain structures[244,245] have been imaged by PFM with nanoscale resolution. The electrically biased tip in PFM can also be used to manipulate ferroelectric properties, such as local polarization, with high precision[246,247]. By tuning the tip bias, multiple parameters such as the piezo coefficients, disorder potential, energy dissipation, nucleation bias and coercive bias can be locally inferred from hysteresis loops[248]. In order to track the dynamics of the ferroelectric domain structure, stroboscopic PFM was developed to measure fast snapshots with nanosecond time resolution, from which the nucleation rate or the mobile velocity of domain walls were extracted[249]. As PFM is only sensitive to the strength of electric fields, the combination of PFM with magnetic force microscopy[250] or scanning magnetometry[251] opens up the possibility of simultaneous imaging of ferroelectric and ferromagnetic ordering, which provides microscopic insight into the coupling of ferroelectric and non-collinear antiferromagnetic domains.

Examples from biology

Imaging biological systems at work. AFM is most often used in biology as an imaging technique[24], widely applied to various biological systems ranging from organs, tissues, cells, organelles and membranes to proteins and nucleic acids. The (sub)structural details of single native proteins or nucleic acids can be directly imaged at (sub)nanometre resolution[24,252–254] (FIG. 9a–c). Because cells, bones, tissues and organs have rough surfaces that are softer than the silicon nitride tip used in AFM, they deform easily and interact with larger areas of the tip apex and side. Such samples are imaged at lower resolution, approaching a few tens of nanometres, with the topographies often showing imaging artefacts[24,255] (FIG. 9d–f).

Imaged in time-lapse mode, biosystems can be observed at work[256], including migrating and dividing cells[257], assembly of actin filaments or collagen fibrils[258], chaperones[259], human communication channels[260], ion channels[261] or uncoiling DNA molecules[253,262,263] (FIG. 9g,h). High-speed AFM allows the monitoring of biological systems at millisecond time resolution, as well as to directly film, for example, dividing bacteria[264], light-driven proton pumps[265], motor proteins[263], immunoglobulins[266], ATP-driven enzymes[267], endosomal sorting complexes[268], nuclear pore complexes[269], channels[119], transporters[270] or CRISPR–Cas9 (REF.[271]) at work. Reducing the high-speed AFM image acquisition to a single position, biomolecular dynamics can be detected

at microsecond time resolution[272]. However, the force applied by the AFM tip while contouring the biological system has to be carefully controlled as the imaging process can quickly (ir)reversibly deform the sample. Nevertheless, a precisely controlled AFM tip can be used to observe force-induced conformational changes of membrane proteins[256,273,274], to dissect DNA[275] or protein[276] complexes, or even to manipulate and design biological systems[277]. Such force control of the AFM tip is made easy by a wide variety of AFM imaging modalities, force-feedback controls, and soft and fast-reacting AFM cantilevers[24,29,278,279].

Manipulation and spectroscopy. The ability to mechanically manipulate biological samples by the AFM tip has raised the issues of measuring the forces interacting between the AFM tip and sample and those interacting between biological samples[280]. Force–distance curves can be used to quantify the hydrophobic, hydrophilic, electrostatic, van der Waals, Young's modulus, energy dissipation and many other physical properties of the sample surface, provided that the properties of the AFM tip have been defined by, for example, characterizing a reference sample. Sometimes, the tip is replaced by a micrometre-sized bead to probe the mechanical properties of larger surface areas of cells or tissues[281]. Examples encompass measuring the elastic properties of the cell cortex, neuronal tissues or even organs of living animals[34]. However, to properly analyse the elastic properties of a soft heterogeneous sample indented by a sharp tip requires the application of theoretical models such as Hertz theory or similar models, which have limitations and must be applied with care[34,282]. One way to circumvent such limitations is to use a bare AFM cantilever without the tip in a parallel plate assay, which has shown that mammalian cells measure confining distances of their surrounding environment[283] and round up for mitosis by generating hydrostatic pressure[284,285]. The physical properties, measured as force–distance or force–time curves, depend on the speed or time at which they are probed by AFM[34]. Consequently, the elastic properties of biological systems probed at various speeds can differ considerably[286,287]. To properly describe the mechanical properties of a biological sample relies on the characterization of these properties over a wide range of speeds, which leads towards describing the free-energy landscape of biomolecular bonds or the rheological properties of cells[34]. Approaches that probe the time dependency of mechanical properties can provide detailed insight into the non-linear active and passive viscoelastic response of biological systems to mechanical stimuli[257,287] or the non-linear characteristic behaviour of biological bonds[288,289].

Using single-molecule force spectroscopy to measure specific forces between an AFM tip and a biological system or between two biological systems requires tip functionalization[31] (BOX 2). Single-molecule force spectroscopy is currently used as a tool to characterize the binding of many different receptor–ligand interactions, the stretching of polypeptides, nucleic acids or sugars, or the unfolding of water-soluble and membrane proteins. Single-molecule force spectroscopy has been used

to characterize biochemical bonds or interactions in and out of equilibrium[290,291].

In single-cell force spectroscopy, the tip of the AFM cantilever is replaced by a living cell to probe cellular interactions with the environment[292]. Single-cell force spectroscopy is particularly fascinating to learn how cells initiate and strengthen adhesion to their environment, including extracellular molecules, viruses, cells, tissues,
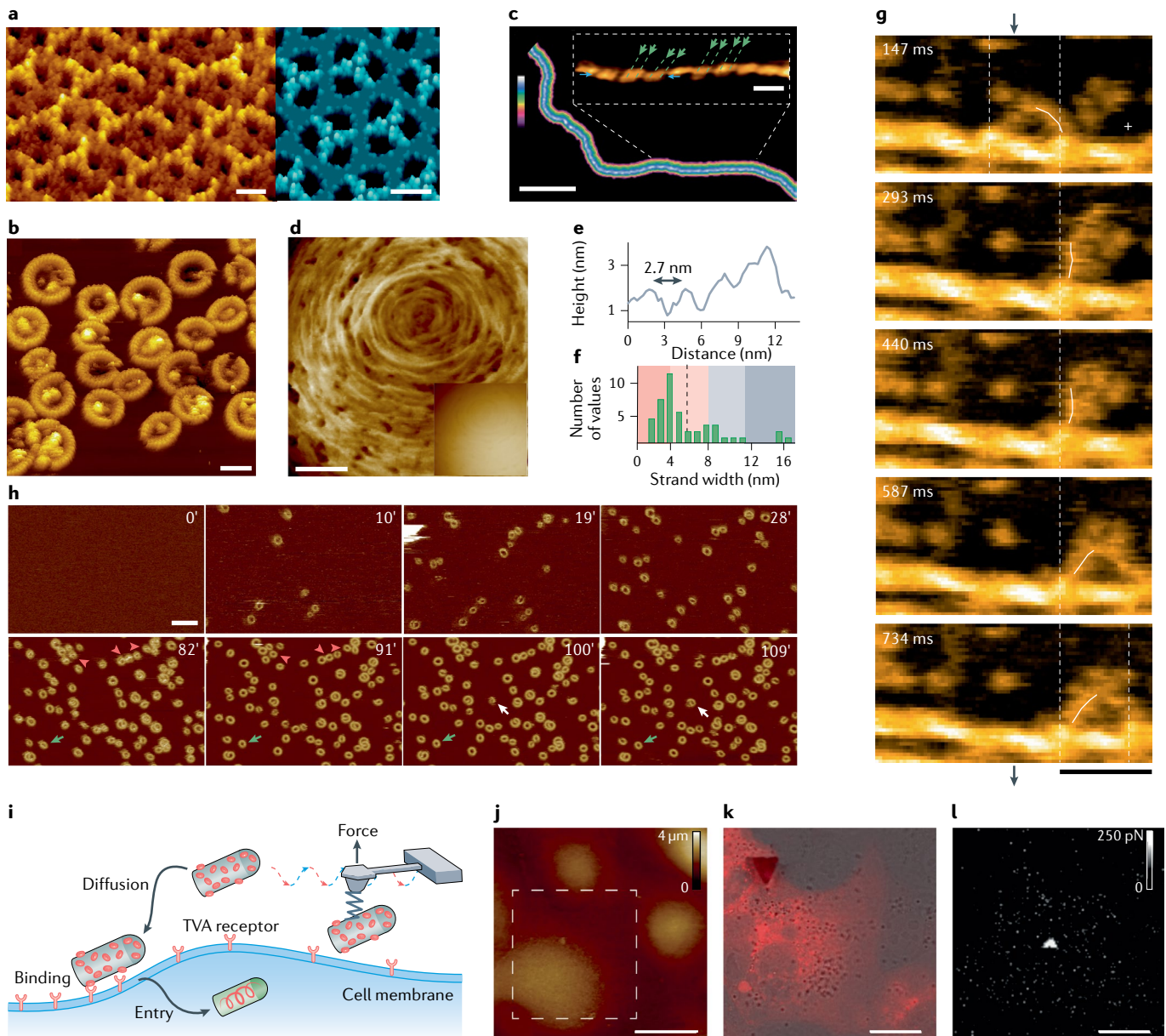

Fig. 9 | **High-resolution atomic force microscopy imaging of biological systems. a** | Periplasmic surface of outer membrane protein OmpF, of which structural details imaged by atomic force microscopy (AFM) resemble the atomistic model (blue). Scale bar = 50 Å. **b** | Human gasdermin D (GSDMD^Nterm) forming lytic transmembrane pores. Scale bar = 20 nm. **c** | Plasmid DNA displayed in false colours. Inset: left-handed double helix. Scale bar = 50 nm; inset scale bar = 10 nm. **d** | High-pass filtered AFM image (inset shows raw data) of the peptidoglycan layer of *Staphylococcus aureus*. Scale bar = 100 nm. **e** | Typical height profile showing spacing between peptidoglycan strands imaged by AFM. **f** | Width of peptidoglycan strands imaged by AFM. Dashed line indicates mean. **g** | High-speed AFM showing hand over hand movement of the motor protein myosin in 1 µM ATP. Arrowhead indicates streptavidin, white line shows the swinging lever, dashed lines show centre of the mass of the motor domains. Image width represents 130 nm. **h** | Time-lapse AFM of GSDMD^Nterm forming lytic pores. The topographs, taken at different time points indicated in minutes, follow GSDMD^Nterm membrane insertion and assembly. White, green and red arrows indicate the reassembly of different GSDMD^Nterm oligomers. Scale bar = 50 nm. **i** | Schematic of force–distance curve-based AFM detecting binding of a rabies virus while imaging a living mammalian cell. Force–distance curve-based AFM tethers the virus to the AFM tip via a long PEG-linker and detects for every pixel of the topograph whether the virus binds to the cell surface. **j** | Force–distance curve-based AFM topograph of cells recorded using the virus-functionalized AFM tip. Scale bar = 20 µm. **k** | Superposition of fluorescence (TVA–mCherry) and differential interference contrast images recorded at the dashed square in part **j**. Scale bar = 10 µm. **l** | Corresponding adhesion image showing specific adhesion events of the virus-functionalized tip. Scale bar = 10 µm. Part **a** adapted with permission from REF.[252], Elsevier. Part **b** reprinted with permission from REF.[253], Wiley. Part **c** reprinted with permission from REF.[254], ACS. Parts **d**–**f** adapted from REF.[255], Springer Nature Limited. Part **g** adapted from REF.[263], Springer Nature Limited. Part **h** reprinted with permission from REF.[253], Wiley. Parts **i**–**l** adapted from REF.[294], Springer Nature Limited.

Box 2 | **Tip functionalization for biological applications**

For biological atomic force microscopy (AFM)-based force spectroscopy, tip functionalization is crucial as it permits engaging the tip in specific interactions with molecules of interest. Although picking up molecules non-specifically using a bare AFM tip or using a gold-coated AFM tip to covalently bind cysteines is possible[321], a plethora of methods have been developed to graft specific molecules of interest for recognition force spectroscopy or recognition imaging[322] to the AFM tip[323]. The most commonly used strategy entails covalent linkage of the probe molecule to the AFM tip via a PEG-linker[324]. Using a PEG-linker between the tip and the probe molecule has two main advantages: it provides a spacer distance between the tip and the surface, thereby minimizing non-specific tip–sample interactions, and it results in a typical PEG-stretching fingerprint in force–distance curves, which serves as a signature of specific recognition events. For protein unfolding experiments, ultra-stable biological bonds such as cohesion–dockerin — the latter engineered into the sample protein — allow covalent binding of both interaction partners to the surface and the tip, because this covalent bond is stronger than the interaction being measured, and its unbinding creates a recognizable signature in the force curves[289,325].

Chemically functionalizing the AFM tip with a ligand, receptor or (bio)chemical compound allows force–volume or force–distance curve-based AFM to simultaneously record the topography and to map a specific biologically relevant interaction between the functionalized tip and the biological sample at every sample surface position[33,326]. Recorded in time-lapse mode, one can even observe living biological systems actively changing manifold physical and (bio)chemical properties[257,284,326]. For example, functionalizing an AFM tip with chemical groups has enabled the mapping of functional nanodomains on living cell surfaces[327], the binding steps and parameters of rabies viruses to mammalian cells[294] or the free-energy landscape of ligands binding to human G-protein-coupled receptors[328]. Differentiating binding of two different ligands functionalizing the same AFM tip to a GPCR has also been demonstrated[329].

bones, organs or biomaterials[293]. Taking the force spectra at every pixel during scanning enables simultaneous measurement of sample topography and related maps of mechanical adhesion, deformation, elasticity and dissipation[294] (FIG. 9i–l).

Cantilever-based sensing. Beyond imaging, cantilever array technologies are excellent chemical and biomedical nanosensors, which can convert the specific or unspecific adsorption of molecules to the cantilever into nanomechanical motion[295]. Applications of nanosensors include detecting DNA hybridization with single point mutation sensitivity, recognizing proteins and antibodies, assessing patient eligibility for cancer treatment or detecting multidrug-resistant bacteria, which cause considerable morbidity, mortality and health-care costs[32,296].

The dysregulation of size, volume and mass in living cells gives rise to many diseases. Several microcantilever-based technologies have been developed to monitor the mass of single cells with unprecedented accuracy. In one approach, suspended cells are floating through a hollow cantilever exposed to a vacuum and, upon passing the free cantilever end, their buoyant mass is measured. The high mass resolution approaching several femtograms makes this approach particularly suitable to monitor small cells such as yeast at repeating time points[297]. In another approach, the cantilever immersed in buffer solution and exposed to cell culture conditions continuously monitors the total (inertial) mass of larger mammalian cells adhering to the free cantilever end at millisecond time resolution over the course of days[298]. The combination of both approaches with modern light microscopy enables optical imaging of biological

Cantilever array technologies
Technologies using arrays of cantilevers for detecting the chemical reactions and nanomechanical motion of biomolecules with high sensitivity.

processes inside the cell and monitoring their link to cell volume regulation and growth.

Reproducibility and data deposition

For SPM applied across physics, chemistry and material sciences, the results are relatively easy to reproduce, especially for those under the UHV condition, owing to well-controlled tip and surface conditions. However, in ambient and liquid conditions, reproducibility is unfortunately poorer, likely owing to noise in liquid and at room temperature, uncertainties of the tip apex and possible contamination of the tip and the surface. Such problems are probably most prominent for the adoption of SPM in biology, which has very complicated environment and deals with sophisticated biological samples, and lead to a lag in establishing reproducibility, field standards and data sharing.

Reproducibility

SPM is a young technique and, thus, is still technically improving a lot. Therefore, wider reproducibility would require many users to have access to state-of-the-art machines, which is difficult to achieve in a field where many laboratories operate prototype devices and customized variations. Specifically, in different prototypes from different laboratories, the routines for operation, the techniques for data acquisition, the treatments for the tip apex and surface, and the post-process and analysis strategies for raw data have big discrepancies, leading to limited reproducibility for general users. Another related problem is that acquiring state-of-the-art data still demands technical insights and the skills of a specialist, because users should have the requisite experience and critical understanding to recognize tip and surface quality, to choose the appropriate imaging parameters and to rule out imaging artefacts. Over recent years, we have seen the emergence of several operational modes that alleviate manual operation problems and automatically propose operational parameters, such as ScanAsyst and similar modes. Unfortunately, these modes are manufacturer-specific and the resulting data are not reproducible with different devices.

The cleanness and robustness of sample surfaces are very important to achieve good reproducibility. Under the UHV environment, a clean surface of the sample can be easily obtained and maintained by cycles of ion sputtering and thermal annealing. By contrast, the surface under liquid and ambient conditions can easily be contaminated or chemically changed. So far, there is almost no efficient and reversible control of the sample state, which can change during sample preparation or SPM imaging. In the worst case, it may be difficult to determine which topography corresponds to which cell state.

Several challenges had to be overcome to enable the imaging of biological systems in their native state. First, AFM sample preparation procedures had to be developed to ensure the native state of the biological system. The challenge was achieved by, for example, adsorbing biological samples in physiologically relevant buffer solutions and temperatures to chemically inert supports such as hydrophilic mica that would not impair their functionality. Second, the native state of the sample

had to be maintained during AFM measurement, which mostly is provided by buffer solution and controlled environmental systems (temperature, humidity and gas). Third, AFM technology and imaging conditions had to be developed to avoid unwanted perturbation of the soft biological system contoured by the mechanically scanning AFM tip. Structurally and functionally well-characterized reference samples served valuably to optimize AFM set-up and imaging conditions such as cantilever properties, tip radius and material, imaging force and other imaging parameters.

Finally, and likely most importantly, SPM reproducibility relies a lot on tip qualities such as the sharpness, aspect ratio and symmetry of the tip apex, directly affecting the surface contouring accuracy and, thus, the imaging result. Finding ways to reproducibly generate high-quality tips is thus a prerequisite for data reproducibility in the field. For UHV experiments, an atomically sharp tip can be readily obtained by in situ tip treatments such as controlled poking and field emission during the scanning. The tip condition is usually judged by the characteristic features of known atoms, molecules or surface reconstructions. The ways to functionalize the tip by single atoms or molecules and to manipulate single atoms or molecules are also well established. Such mature procedures mentioned above are popularly applied for obtaining the atomically resolved images and STS on surfaces of different single crystals such as Au(111), Si(111) and graphite, all of which are standard samples for characterizing SPM function and to ensure the acquisition of high-quality images and STS spectra.

Field standards on open data

In both the electron microscopy and X-ray crystallography fields, data acquisition tables and data processing methods are published alongside structures. This is unfortunately not the case for the SPM field. Establishing general standards such as data formats and the strategies of data processing and image reconstruction should be a major ambition. In AFM-based force spectroscopy, standardization of methods to characterize and calibrate the cantilever and the sensitivity of the optical lever system, the ensemble signal response of the laser and the optical path that documents the cantilever deflection has been established[299,300]. In imaging, the multitude of operational modes makes establishing generalizable field standards difficult. Although individual companies and laboratories have evolved powerful methods for image acquisition, raw data are not easily shareable within the community and the analysis tools and data representation are today not standardized. Images and derived AFM structures could and should be encoded in a common file format such as .dat, which would allow efficient database deposition, interchange, cross-evaluation, comparison and model-based validation of data.

Minimum reporting standards. Researchers should provide in their methods section a clear description of the AFM set-up used, the AFM mode applied and the operation details of the applied mode. Basic details regarding the cantilevers of use are also expected, such as the geometrical dimensions, shape, material, spring constant resonance frequency and quality factor. Finally, knowledge about the tip shape should be provided. For biological applications, the environmental conditions, precise buffer conditions, temperature and how the sample was treated before and throughout the experiment are of equal importance.

Limitations and optimizations
Tip disturbance

One common intrinsic limitation of all SPM is that the tip will inevitably perturb the surface as well as any adsorbates; this is due to the excitation of the tunnelling current and the interaction force between the tip and the surface. Therefore, the acquired images may not reflect the real structure and dynamics. This problem becomes particularly serious for weakly bonded systems and under high-resolution imaging conditions, where the tip is usually brought very close to the surface. One straightforward way to reduce tip disturbance is by enhancing detection sensitivity and using only a small current and force for imaging. In SPM under UHV conditions, the CO-terminated tip allows the imaging of metastable structures in a nearly non-invasive manner owing to the ultra-high flexibility of the tip apex and the weak higher-order electrostatic force[54]. Recently, a single nitrogen vacancy centre in proximity to the surface of a high-quality diamond tip is promising to sense extremely weak magnetic fields through magnetic dipole interactions, such as proton spin fluctuations[301]. Nevertheless, tip disturbance is not always unfavourable and does not always need to be avoided. It can be used as a stimulus to measure the mechanical, magnetic, optical and electrical responses of the surface or to manipulate the sample. In biological AFM, improved FM-AFM and amplitude modulation AFM and non-resonant modes with faster and more sensitive feedback operation enable sufficient control of applied force to image biological samples. Researchers have used comparison with molecular structures and internal molecular symmetry (if present) to assess the non-invasiveness of AFM scanning[120].

Limited temporal resolution

Despite unprecedented spatial resolution down to the atomic scale, the traditional temporal resolution of SPM is limited by the bandwidth of electronics for signal acquisition and the resonance frequency of the scanner head, typically in the order of microseconds. It is possible to improve the temporal resolution by using wideband preamplifiers, fast analogue to digital converters, small and rigid scanners, and fast feedback systems[61,302]. In this way, the scanning speed can be increased above 100 frames per second, which is video-rate SPM[15]. In order to further push the temporal resolution of signal detection to picoseconds or even femtoseconds, SPM must be combined with ultra-fast pump-probe technology, by coupling the tip–surface junction with pulsed electric waves, terahertz pulses and near-infrared and visible lasers[63–66,130]. The key feature is that the optical or electric pulses are employed to pump the electronic states of sample to a higher energy level, whereas the response and the relaxation dynamics

are locally probed by the tip–surface interactions, either pulsed or continuous, to ensure the atomic spatial resolution. The temporal resolution is basically given by the delay time between the optical or electric pulses, thus defeating the intrinsic limitation from the SPM electronics and mechanics. Tracking and control of the ultra-fast electronic processes on the atomic scale even with attosecond resolution has recently been demonstrated[303].

Insensitivity to the buried interface

As a surface-sensitive technique, SPM cannot readily access the buried interfaces. This is because low-energy tunnelling electrons cannot penetrate through thick layers, and high spatial resolution usually relies on the short-range tip–surface interaction. Cross-section SPM provides a solution to access interfacial information, by breaking the sample apart and positioning the tip on the cross-section of the sample[304]. Such a technique can only gain spatial information along the surface; lateral information is not measured. Scanning gate microscopy has been used to probe the 2D electron gas located at the interface of semiconductor devices[97]. Owing to their excellent penetrability, microwaves emitted by the SPM tip are used to map out the dielectric response of interfacial materials by detecting the S/T parameters of near-field microwaves[105]. However, the spatial resolution of these methods is limited because of the large distance between the tip and the target interface, as well as the slow decay of the microwave and electric fields on the tip. Integration of a super lens to SNOM allows the investigation of buried interfaces as deep as hundreds of nanometres while still maintaining the nanoscale spatial resolution[305].

Outlook
Coherent detection and control

Imaging by SPM methods relies on various tip–surface interactions. However, the quantum coherence could be easily destroyed by such interactions as the tunnelling current, force, electron and/or phonon scattering, and charge and/or spin noise. In addition, many coherent processes occur at ultra-fast timescales, beyond the temporal resolution of conventional SPM. Therefore, most of the results obtained by SPM reflect only incoherent processes. Following coherent evolution and achieving coherent control on various quantum processes is one of most challenging but fascinating future directions for SPM. SPM combined with nitrogen vacancy technology provides a possible solution[79]. The spin triplet states of the nitrogen vacancy could be excited and coherently manipulated through microwave pulses. The magnetic information near the nitrogen vacancy can be stored during the coherent evolution of nitrogen vacancy states through dipolar interaction, and finally read out by spin-dependent fluorescence[306]. Because of its inert host and long coherence time, the nitrogen vacancy could be powerful even under an ambient environment[307]. Integrating SPM with a nitrogen vacancy quantum sensor (nitrogen vacancy-based SPM) is able to quantitatively image and precisely control the coherent behaviours of target spins with nanoscale resolution. The detection is non-perturbative because of the weak

coupling strength between the nitrogen vacancy and the sample[308,309]. Choosing qPlus-based non-contact AFM will further optimize the coherence and sensitivity of such a quantum sensor in nitrogen vacancy-based SPM[310]. The coupling of STM with different electromagnetic waves also provides unique opportunities to detect the coherent spin, electron and phonon dynamics at different timescales. Indeed, imaging and coherent control of electron spins with atomic resolution has been achieved by ESR-STM[77], where the spin dynamics is driven by radio-frequency bias. In addition, the coherent vibration dynamics of single molecules at the picosecond scale can be monitored through terahertz STM[66]. By coupling a femtosecond laser with STM, it has been possible to track ultra-fast dynamics such as the temperature-transient charge carrier[63], dependent spin relaxations in gallium arsenide[64] and the coherent vibration-driven conformational changes of single molecules[151]. Very recently, coherent control of electrons even at attosecond resolution has also been demonstrated[303].

Three-dimensional imaging

SPM has been very successful in imaging samples in two dimensions, where the sample surface needs to be atomically flat to ensure high-resolution and stable imaging. However, when the target objects have a relatively rough surface, the imaging resolution and quality usually decline[311]. Unfortunately, atomically flat surfaces are only available for simple model systems, whereas 3D samples are more ubiquitous. These include large biomolecules, clusters, porous materials, nanostructured surfaces and so on. It is therefore imperative to develop new SPM techniques capable of atomic imaging in 3D.

One avenue for achieving 3D imaging is measuring height-dependent current and force curves at every pixel and plotting the current and force data in *xyz* directions. For example, the 3D force mapping of water–solid interfaces by FM-AFM provides microscopic insight into the interfacial structure of hydration layers[90,167,312]. Other examples contour the rather rough surfaces of complex biological systems in 3D and at the same time map their mechanical properties. However, such approaches are time-consuming and suffer from thermal drift because of the need for long-term data acquisition. A simpler method — which also improves resolution — is to apply height compensation either by opening the current feedback loop simultaneously during the signal acquisition or by automatically adjusting the tip height according to pre-acquired tomography information to make the tip follow the geometric contour of the 3D objects[313]. With such methods, the step structure of semiconductor surfaces, C_{60} (REF.[313]) and other non-planar molecules with complex 3D geometry[314] have been visualized with submolecular resolution.

Recently, a remarkable achievement was made in molecular 3D structure reconstruction from 3D SPM data sets using machine learning based on convolutional neural networks[315], which can learn an approximation for image inversion efficiently using such a universal fitting scheme. However, one of the biggest challenges lies in the insufficient amounts of data sets from realistic SPM experiments needed for image inversion

of 3D molecular structure processes. Another way to image 3D structure is similar to the idea of magnetic resonance imaging[316]. The SPM tip with a high field gradient may be used to select a certain thin slice of the 3D samples, such that the electronic, vibrational or spin signals within this specific slice can be read out by far-field photons. The combination of optical microcavity with SPM may also provide new possibilities of sensing the internal information in 3D structure using an optomechanical response, such as ultrasonic measurements[317].

SPM under extreme conditions

Under extreme conditions, such as ultra-low and ultra-high temperatures, strong magnetic fields and ultra-high pressure, many interesting and unexpected phenomena will emerge, beyond our conventional knowledge of more standard conditions. To date, the atomic or nanoscale understanding of material properties under various extreme conditions is far from complete, calling for the development of SPM that is compatible with various extreme conditions.

STM has been successfully combined with a dilution fridge, which can lower the base temperature to 10 mK (REF.[13]) and provide an ultra-high magnetic field up to 30 T (REF.[14]). The highest electronic energy resolution could achieve ~10 μeV (REFS[13,22]), which is limited by the efficient electron temperature instead of the absolute base temperature. The key issues are how to isolate the vibration from the dilution fridge and to lower the electronic temperature by proper radio-frequency shielding. Recently, qPlus-AFM was also incorporated into a dilution fridge with magnetic field up to 7 T, which opens up new capabilities in studying electronic devices[22]. SPM working at ultra-low temperature and ultra-high magnetic field is expected to address exotic quantum effects with unprecedented details in both real space and energy space, such as superconductivity, the quantum Hall effect and strongly correlated physics.

Many chemical reactions and material growth reactions occur at elevated temperatures. High-temperature SPM is a useful operando technique to monitor those dynamic processes with atomic resolution[318]. The most challenging problems remaining for high-temperature SPM are thermal drift and mechanical stability. In addition, the rapid degradation of the tip and scanner

materials at high temperature under a high-pressure gas environment also limits its performance. Recently, some new techniques have been introduced to suppress drifting and enhance stability. One of the efficient solutions is developing video-rate SPM systems where the fast dynamics in chemical reactions are captured within milliseconds with little impact from temperature fluctuations[15]. For example, real-time monitoring of the atomic growth of graphene has been realized by video-rate STM at 710 K (REF.[15]).

SPM of living systems

Compared with most optical microscopies, SPM-based approaches can image living biological systems with an unprecedentedly low signal to noise ratio. However, owing to the increasing complexity of such living systems, the user is often challenged to identify specific cellular features and must either compare the sample topography with known morphologies (for example, structural references) or combine SPM with fluorescence microscopy, where a subset of structural details has been fluorescently labelled. AFM-based functional imaging may be the answer; this technique uses the AFM tip as a nanoscopic tool that can simultaneously image, quantify, morphologically map and manipulate specific interactions of biological moieties[24,31]. Biological systems are highly dynamic and can actively or passively change state within milliseconds to minutes. Thus, the state of complex biosystems imaged by SPM must be monitored and should not be altered by, for example, the sample preparation procedure, including features such as drying, adsorption of a 3D object onto a support, non-physiological temperature or a buffer solution. If all of the SPM parameters are adjusted properly, biological systems can be observed at work by time-lapse or high-speed video SPM. However, other microscopic approaches such as cryogenic transmission electron microscopy can provide snapshots of biological systems at work in 3D at atomistic resolution. Thus, SPM as a surface technique may be a tool for examining niches not addressable by any other technique, such as simultaneously imaging biological systems at work at nanometre resolution and characterizing their various mechanical, chemical and biological properties[24,34,277].

Published online: 13 May 2021

1. Binnig, G., Rohrer, H., Gerber, C. & Weibel, E. Surface studies by scanning tunneling microscopy. *Phys. Rev. Lett.* **49**, 57–61 (1982). **This work reports the first atomically resolved image of conductive surfaces with STM.**
2. Binnig, G., Quate, C. F. & Gerber, C. Atomic force microscope. *Phys. Rev. Lett.* **56**, 930–933 (1986). **This work develops AFM for probing non-conductive surfaces.**
3. Quate, C. F. Vacuum tunneling — a new technique for microscopy. *Phys. Today* **39**, 26–33 (1986).
4. Lortscher, E., Widmer, D. & Gotsmann, B. Next-generation nanotechnology laboratories with simultaneous reduction of all relevant disturbances. *Nanoscale* **5**, 10542–10549 (2013).
5. Besocke, K. An easily operable scanning tunneling microscope. *Surf. Sci.* **181**, 145–153 (1987).
6. Pan, S. H., Hudson, E. W. & Davis, J. C. He-3 refrigerator based very low temperature scanning tunneling microscope. *Rev. Sci. Instrum.* **70**, 1459–1463 (1999).

7. Gerber, C., Binnig, G., Fuchs, H., Marti, O. & Rohrer, H. Scanning tunneling microscope combined with a scanning electron-microscope. *Rev. Sci. Instrum.* **57**, 221–224 (1986).
8. Oliva, A. I., Romero, A., Pena, J. L., Anguiano, E. & Aguilar, M. Electrochemical preparation of tungsten tips for a scanning tunneling microscope. *Rev. Sci. Instrum.* **67**, 1917–1921 (1996).
9. Zhang, R. et al. Chemical mapping of a single molecule by plasmon-enhanced Raman scattering. *Nature* **498**, 82–86 (2013).
10. Crommie, M. F., Lutz, C. P. & Eigler, D. M. Confinement of electrons to quantum corrals on a metal-surface. *Science* **262**, 218–220 (1993). **This article demonstrates the ability of manipulating atoms and constructing artificial quantum structures.**
11. Eigler, D. M. & Schweizer, E. K. Positioning single atoms with a scanning tunneling microscope. *Nature* **344**, 524–526 (1990).

12. Stroscio, J. A. & Eigler, D. M. Atomic and molecular manipulation with the scanning tunneling microscope. *Science* **254**, 1319–1326 (1991).
13. Assig, M. et al. A 10 mK scanning tunneling microscope operating in ultra high vacuum and high magnetic fields. *Rev. Sci. Instrum.* **84**, 033903 (2013).
14. Meng, W. et al. 30 T scanning tunnelling microscope in a hybrid magnet with essentially non-metallic design. *Ultramicroscopy* **212**, 112975 (2020).
15. Patera, L. L. et al. Real-time imaging of adatom-promoted graphene growth on nickel. *Science* **359**, 1243–1246 (2018).
16. Eren, B. et al. Activation of Cu(111) surface by decomposition into nanoclusters driven by CO adsorption. *Science* **351**, 475–478 (2016).
17. Pfisterer, J. H. K., Liang, Y. C., Schneider, O. & Bandarenka, A. S. Direct instrumental identification of catalytically active surface sites. *Nature* **549**, 74–77 (2017).

18. Meyer, G. & Amer, N. M. Novel optical approach to atomic force microscopy. *Appl. Phys. Lett.* **53**, 1045–1047 (1988).

19. Drake, B. et al. Imaging crystals, polymers, and processes in water with the atomic force microscope. *Science* **243**, 1586–1589 (1989).

20. Martin, Y., Williams, C. C. & Wickramasinghe, H. K. Atomic force microscope force mapping and profiling on a sub 100-Å scale. *J. Appl. Phys.* **61**, 4723–4729 (1987).

21. Hansma, P. K. et al. Tapping mode atomic-force microscopy in liquids. *Appl. Phys. Lett.* **64**, 1738–1740 (1994).

22. Schwenk, J. et al. Achieving μeV tunneling resolution in an in-operando scanning tunneling microscopy, atomic force microscopy, and magnetotransport system for quantum materials research. *Rev. Sci. Instrum.* **91**, 071101 (2020).

23. Herruzo, E. T., Perrino, A. P. & Garcia, R. Fast nanomechanical spectroscopy of soft matter. *Nat. Commun.* **5**, 3126 (2014).

24. Dufrene, Y. F. et al. Imaging modes of atomic force microscopy for application in molecular and cell biology. *Nat. Nanotechnol.* **12**, 295–307 (2017).

25. Ando, T., Uchihashi, T. & Kodera, N. High-speed AFM and applications to biomolecular systems. *Annu. Rev. Biophys.* **42**, 393–414 (2013).

26. Ohnesorge, F. & Binnig, G. True atomic-resolution by atomic force microscopy through repulsive and attractive forces. *Science* **260**, 1451–1456 (1993).

27. Giessibl, F. J. Atomic-resolution of the silicon (111)-(7 × 7) surface by atomic-force microscopy. *Science* **267**, 68–71 (1995).

28. Giessibl, F. J. The qPlus sensor, a powerful core for the atomic force microscope. *Rev. Sci. Instrum.* **90**, 011101 (2019).

29. Bull, M. S., Sullan, R. M. A., Li, H. B. & Perkins, T. T. Improved single molecule force spectroscopy using micromachined cantilevers. *ACS Nano.* **8**, 4984–4995 (2014).

30. Florin, E. L., Moy, V. T. & Gaub, H. E. Adhesion forces between individual ligand–receptor pairs. *Science* **264**, 415–417 (1994).

31. Muller, D. J. & Dufrene, Y. F. Atomic force microscopy as a multifunctional molecular toolbox in nanobiotechnology. *Nat. Nanotechnol.* **3**, 261–269 (2008).

32. Huber, F., Lang, H. P., Backmann, N., Rimoldi, D. & Gerber, C. Direct detection of a BRAF mutation in total RNA from melanoma cells using cantilever arrays. *Nat. Nanotechnol.* **8**, 125–129 (2013).

33. Dufrene, Y. F., Martinez-Martin, D., Medalsy, I., Alsteens, D. & Muller, D. J. Multiparametric imaging of biological systems by force-distance curve-based AFM. *Nat. Methods* **10**, 847–854 (2013).

34. Krieg, M. et al. Atomic force microscopy-based mechanobiology. *Nat. Rev. Phys.* **1**, 41–57 (2019).

35. Gunther, P., Fischer, U. & Dransfeld, K. Scanning near-field acoustic microscopy. *Appl. Phys. B* **48**, 89–92 (1989).

36. Giessibl, F. J. High-speed force sensor for force microscopy and profilometry utilizing a quartz tuning fork. *Appl. Phys. Lett.* **73**, 3956–3958 (1998).
This work pioneers qPlus-based AFM, which was demonstrated to surpass the spatial resolution of STM.

37. Repp, J., Meyer, G., Stojkovic, S. M., Gourdon, A. & Joachim, C. Molecules on insulating films: scanning-tunneling microscopy imaging of individual molecular orbitals. *Phys. Rev. Lett.* **94**, 026803 (2005).

38. Heinrich, A. J., Gupta, J. A., Lutz, C. P. & Eigler, D. M. Single-atom spin-flip spectroscopy. *Science* **306**, 466–469 (2004).

39. You, S., Lu, J. T., Guo, J. & Jiang, Y. Recent advances in inelastic electron tunneling spectroscopy. *Adv. Phys. X* **2**, 907–936 (2017).

40. Butt, H. J., Cappella, B. & Kappl, M. Force measurements with the atomic force microscope: technique, interpretation and applications. *Surf. Sci. Rep.* **59**, 1–152 (2005).

41. Bartels, L., Meyer, G. & Rieder, K. H. Basic steps of lateral manipulation of single atoms and diatomic clusters with a scanning tunneling microscope tip. *Phys. Rev. Lett.* **79**, 697–700 (1997).

42. Lee, H. J. & Ho, W. Single-bond formation and characterization with a scanning tunneling microscope. *Science* **286**, 1719–1722 (1999).

43. Ho, W. Single-molecule chemistry. *J. Chem. Phys.* **117**, 11033–11061 (2002).

44. Jiang, Y., Huan, Q., Fabris, L., Bazan, G. C. & Ho, W. Submolecular control, spectroscopy and imaging of bond-selective chemistry in single functionalized molecules. *Nat. Chem.* **5**, 36–41 (2013).

45. Ternes, M., Lutz, C. P., Hirjibehedin, C. F., Giessibl, F. J. & Heinrich, A. J. The force needed to move an atom on a surface. *Science* **319**, 1066–1069 (2008).

46. Hopkins, L. C., Griffith, J. E., Harriott, L. R. & Vasile, M. J. Polycrystalline tungsten and iridium probe tip preparation with a Ga+ focused ion-beam. *J. Vac. Sci. Technol. B* **13**, 335–337 (1995).

47. Chen, C. J. Microscopic view of scanning tunneling microscopy. *J. Vac. Sci. Technol. A* **9**, 44–50 (1991).

48. Stockle, R. M., Suh, Y. D., Deckert, V. & Zenobi, R. Nanoscale chemical analysis by tip-enhanced Raman spectroscopy. *Chem. Phys. Lett.* **318**, 131–136 (2000).

49. Kurouski, D., Mattei, M. & Van Duyne, R. P. Probing redox reactions at the nanoscale with electrochemical tip-enhanced Raman spectroscopy. *Nano. Lett.* **15**, 7956–7962 (2015).

50. Bartels, L. et al. Dynamics of electron-induced manipulation of individual CO molecules on Cu(111). *Phys. Rev. Lett.* **80**, 2004–2007 (1998).

51. Kichin, G., Weiss, C., Wagner, C., Tautz, F. S. & Temirov, R. Single molecule and single atom sensors for atomic resolution imaging of chemically complex surfaces. *J. Am. Chem. Soc.* **133**, 16847–16851 (2011).

52. Gross, L. et al. High-resolution molecular orbital imaging using a *p*-wave STM tip. *Phys. Rev. Lett.* **107**, 086101 (2011).

53. Gross, L. et al. Bond-order discrimination by atomic force microscopy. *Science* **337**, 1326–1329 (2012).

54. Peng, J. B. et al. Weakly perturbative imaging of interfacial water with submolecular resolution by atomic force microscopy. *Nat. Commun.* **9**, 122 (2018).
This article develops hydrogen-sensitive AFM for probing water molecules with submolecular resolution.

55. Monig, H. et al. Submolecular imaging by noncontact atomic force microscopy with an oxygen atom rigidly connected to a metallic probe. *ACS Nano.* **10**, 1201–1209 (2016).

56. Guo, J. et al. Real-space imaging of interfacial water with submolecular resolution. *Nat. Mater.* **13**, 184–189 (2014).

57. Hapala, P. et al. Mechanism of high-resolution STM/AFM imaging with functionalized tips. *Phys. Rev. B* **90**, 085421 (2014).

58. Muller, D. J., Fotiadis, D., Scheuring, S., Muller, S. A. & Engel, A. Electrostatically balanced subnanometer imaging of biological specimens by atomic force microscope. *Biophys. J.* **76**, 1101–1111 (1999).

59. Uchihashi, T., Kodera, N. & Ando, T. Guide to video recording of structure dynamics and dynamic processes of proteins by high-speed atomic force microscopy. *Nat. Protoc.* **7**, 1193–1206 (2012).

60. Wilson, N. R. & Macpherson, J. V. Carbon nanotube tips for atomic force microscopy. *Nat. Nanotechnol.* **4**, 483–491 (2009).

61. Besenbacher, F., Jensen, F., Laegsgaard, E., Mortensen, K. & Stensgaard, I. Visualization of the dynamics in surface reconstructions. *J. Vac. Sci. Technol. B* **9**, 874–878 (1991).

62. Loth, S., Etzkorn, M., Lutz, C. P., Eigler, D. M. & Heinrich, A. J. Measurement of fast electron spin relaxation times with atomic resolution. *Science* **329**, 1628–1630 (2010).

63. Terada, Y., Yoshida, S., Takeuchi, O. & Shigekawa, H. Real-space imaging of transient carrier dynamics by nanoscale pump-probe microscopy. *Nat. Photonics* **4**, 869–874 (2010).
This work pushes the temporal resolution of STM to an ultra-fast scale by laser-combined STM.

64. Yoshida, S. et al. Probing ultrafast spin dynamics with optical pump-probe scanning tunnelling microscopy. *Nat. Nanotechnol.* **9**, 588–593 (2014).

65. Cocker, T. L. et al. An ultrafast terahertz scanning tunnelling microscope. *Nat. Photonics* **7**, 620–625 (2013).

66. Cocker, T. L., Peller, D., Yu, P., Repp, J. & Huber, R. Tracking the ultrafast motion of a single molecule by femtosecond orbital imaging. *Nature* **539**, 263–267 (2016).

67. Martin, Y. & Wickramasinghe, H. K. Magnetic imaging by force microscopy with 1000-Å resolution. *Appl. Phys. Lett.* **50**, 1455–1457 (1987).

68. Hartmann, U. Magnetic force microscopy. *Annu. Rev. Mater. Sci.* **29**, 53–87 (1999).

69. Kaiser, U., Schwarz, A. & Wiesendanger, R. Magnetic exchange force microscopy with atomic resolution. *Nature* **446**, 522–525 (2007).

70. Wiesendanger, R., Guntherodt, H. J., Guntherodt, G., Gambino, R. J. & Ruf, R. Observation of vacuum tunneling of spin-polarized electrons with the scanning tunneling microscope. *Phys. Rev. Lett.* **65**, 247–250 (1990).
This work develops the first spin-polarized STM, allowing the probing of magnetic properties of surfaces at atomic scale.

71. Wiesendanger, R. Spin mapping at the nanoscale and atomic scale. *Rev. Mod. Phys.* **81**, 1495–1550 (2009).

72. Vu, L. N., Wistrom, M. S. & Vanharlingen, D. J. Imaging of magnetic vortices in superconducting networks and clusters by scanning squid microscopy. *Appl. Phys. Lett.* **63**, 1693–1695 (1993).

73. Vasyukov, D. et al. A scanning superconducting quantum interference device with single electron spin sensitivity. *Nat. Nanotechnol.* **8**, 639–644 (2013).

74. Chang, A. M. et al. Scanning Hall probe microscopy. *Appl. Phys. Lett.* **61**, 1974–1976 (1992).

75. Baumann, S. et al. Electron paramagnetic resonance of individual atoms on a surface. *Science* **350**, 417–420 (2015).
This article develops the first ESR-STM for measuring ESR and quantum coherence with atomic precision.

76. Willke, P. et al. Hyperfine interaction of individual atoms on a surface. *Science* **362**, 336–339 (2018).

77. Yang, K. et al. Coherent spin manipulation of individual atoms on a surface. *Science* **366**, 509–512 (2019).

78. Rugar, D., Budakian, R., Mamin, H. J. & Chui, B. W. Single spin detection by magnetic resonance force microscopy. *Nature* **430**, 329–332 (2004).

79. Balasubramanian, G. et al. Nanoscale imaging magnetometry with diamond spins under ambient conditions. *Nature* **455**, 648–651 (2008).

80. Matey, J. R. & Blanc, J. Scanning capacitance microscopy. *J. Appl. Phys.* **57**, 1437–1444 (1985).

81. Yoo, M. J. et al. Scanning single-electron transistor microscopy: imaging individual charges. *Science* **276**, 579–582 (1997).

82. Nonnenmacher, M., Oboyle, M. P. & Wickramasinghe, H. K. Kelvin probe force microscopy. *Appl. Phys. Lett.* **58**, 2921–2923 (1991).

83. Guthner, P. & Dransfeld, K. Local poling of ferroelectric polymers by scanning force microscopy. *Appl. Phys. Lett.* **61**, 1137–1139 (1992).

84. Gruverman, A., Alexe, M. & Meier, D. Piezoresponse force microscopy and nanoferroic phenomena. *Nat. Commun.* **10**, 1661 (2019).

85. Rabe, J. P. & Buchholz, S. Commensurability and mobility in two-dimensional molecular patterns on graphite. *Science* **253**, 424–427 (1991).

86. Askadskaya, L. & Rabe, J. P. Anisotropic molecular-dynamics in the vicinity of order–disorder transitions in organic monolayers. *Phys. Rev. Lett.* **69**, 1395–1398 (1992).

87. Ciesielski, A. et al. Dynamic covalent chemistry of bisimines at the solid/liquid interface monitored by scanning tunnelling microscopy. *Nat. Chem.* **6**, 1017–1023 (2014).

88. Itaya, K. & Tomita, E. Scanning tunneling microscope for electrochemistry—a new concept for the insitu scanning tunneling microscope in electrolyte-solutions. *Surf. Sci.* **201**, L507–L512 (1988).

89. Fukuma, T., Kobayashi, K., Matsushige, K. & Yamada, H. True molecular resolution in liquid by frequency-modulation atomic force microscopy. *Appl. Phys. Lett.* **86**, 193108 (2005).

90. Fukuma, T., Ueda, Y., Yoshioka, S. & Asakawa, H. Atomic-scale distribution of water molecules at the mica–water interface visualized by three-dimensional scanning force microscopy. *Phys. Rev. Lett.* **104**, 016101 (2010).

91. Korchev, Y. E., Bashford, C. L., Milovanovic, M., Vodyanoy, I. & Lab, M. J. Scanning ion conductance microscopy of living cells. *Biophys. J.* **73**, 653–658 (1997).

92. Korchev, Y. E., Negulyaev, Y. A., Edwards, C. R. W., Vodyanoy, I. & Lab, M. J. Functional localization of single active ion channels on the surface of a living cell. *Nat. Cell Biol.* **2**, 616–619 (2000).

93. Mangold, S., Harneit, K., Rohwerder, T., Claus, G. & Sand, W. Novel combination of atomic force microscopy and epifluorescence microscopy for visualization of leaching bacteria on pyrite. *Appl. Environ. Microb.* **74**, 410–415 (2008).

94. Guillaume-Gentil, O. et al. Force-controlled manipulation of single cells: from AFM to FluidFM. *Trends. Biotechnol.* **32**, 381–388 (2014).

95. Muralt, P. & Pohl, D. W. Scanning tunneling potentiometry. *Appl. Phys. Lett.* **48**, 514–516 (1986).

96. Eriksson, M. A. et al. Cryogenic scanning probe characterization of semiconductor nanostructures. *Appl. Phys. Lett.* **69**, 671–673 (1996).

97. Topinka, M. A. et al. Imaging coherent electron flow from a quantum point contact. *Science* **289**, 2323–2326 (2000).

98. Shiraki, I., Tanabe, F., Hobara, R., Nagao, T. & Hasegawa, S. Independently driven four-tip probes for conductivity measurements in ultrahigh vacuum. *Surf. Sci.* **493**, 633–643 (2001).

99. Baringhaus, J. et al. Exceptional ballistic transport in epitaxial graphene nanoribbons. *Nature* **506**, 349–354 (2014).

100. Lewis, A., Isaacson, M., Harootunian, A. & Muray, A. Development of a 500-Å spatial-resolution light-microscope. 1. Light is efficiently transmitted through λ/16 diameter apertures. *Ultramicroscopy* **13**, 227–231 (1984).

101. Inouye, Y. & Kawata, S. Near-field scanning optical microscope with a metallic probe tip. *Opt. Lett.* **19**, 159–161 (1994).

102. Zenhausern, F., Martin, Y. & Wickramasinghe, H. K. Scanning interferometric apertureless microscopy — optical imaging at 10 Angstrom resolution. *Science* **269**, 1083–1085 (1995).

103. Zhang, Y. et al. Visualizing coherent intermolecular dipole–dipole coupling in real space. *Nature* **531**, 623–627 (2016).

104. Wei, T., Xiang, X. D., WallaceFreedman, W. G. & Schultz, P. G. Scanning tip microwave near-field microscope. *Appl. Phys. Lett.* **68**, 3506–3508 (1996).

105. Lai, K., Ji, M. B., Leindecker, N., Kelly, M. A. & Shen, Z. X. Atomic-force-microscope-compatible near-field scanning microwave microscope with separated excitation and sensing probes. *Rev. Sci. Instrum.* **78**, 063702 (2007).

106. Nowak, D. et al. Nanoscale chemical imaging by photoinduced force microscopy. *Sci. Adv.* **2**, e1501571 (2016).

107. Ni, T. et al. Structure and mechanism of bactericidal mammalian perforin-2, an ancient agent of innate immunity. *Sci. Adv.* **6**, eaax8286 (2020).

108. Gross, L., Mohn, F., Moll, N., Liljeroth, P. & Meyer, G. The chemical structure of a molecule resolved by atomic force microscopy. *Science* **325**, 1110–1114 (2009).

109. Guo, J. et al. Nuclear quantum effects of hydrogen bonds probed by tip-enhanced inelastic electron tunneling. *Science* **352**, 321–325 (2016).

110. Necas, D. & Klapetek, P. Gwyddion: an open-source software for SPM data analysis. *Cent. Eur. J. Phys.* **10**, 181–188 (2012).

111. Horcas, I. et al. WSxM: a software for scanning probe microscopy and a tool for nanotechnology. *Rev. Sci. Instrum.* **78**, 013705 (2007).

112. Rigato, A., Rico, F., Eghiaian, F., Piel, M. & Scheuring, S. Atomic force microscopy mechanical mapping of micropatterned cells shows adhesion geometry-dependent mechanical response on local and global scales. *ACS Nano.* **9**, 5846–5856 (2015).

113. Smolyakov, G., Formosa-Dague, C., Severac, C., Duval, R. E. & Dague, E. High speed indentation measures by FV, QI and QNM introduce a new understanding of bionanomechanical experiments. *Micron* **85**, 8–14 (2016).

114. Kuhlbrandt, W. The resolution revolution. *Science* **343**, 1443–1444 (2014).

115. Tang, G. et al. EMAN2: an extensible image processing suite for electron microscopy. *J. Struct. Biol.* **157**, 38–46 (2007).

116. vanHeel, M., Harauz, G., Orlova, E. V., Schmidt, R. & Schatz, M. A new generation of the IMAGIC image processing system. *J. Struct. Biol.* **116**, 17–24 (1996).

117. Shaikh, T. R. et al. SPIDER image processing for single-particle reconstruction of biological macromolecules from electron micrographs. *Nat. Protoc.* **3**, 1941–1974 (2008).

118. Scheres, S. H. W. RELION: implementation of a Bayesian approach to cryo-EM structure determination. *J. Struct. Biol.* **180**, 519–530 (2012).

119. Ruan, Y. et al. Structural titration of receptor ion channel GLIC gating by HS-AFM. *P Natl. Acad. Sci.* **115**, 10333–10338 (2018).

120. Fechner, P. et al. Structural information, resolution, and noise in high-resolution atomic force microscopy topographs. *Biophys. J.* **96**, 3822–3831 (2009).

121. Muller, D. J., Fotiadis, D. & Engel, A. Mapping flexible protein domains at subnanometer resolution with the atomic force microscope. *FEBS Lett.* **430**, 105–111 (1998).

122. Gari, R. R. S. et al. Direct visualization of the *E. coli* Sec translocase engaging precursor proteins in lipid bilayers. *Sci. Adv.* **5**, eaav9404 (2019).

123. Scheuring, S., Rigaud, J. L. & Sturgis, J. N. Variable LH2 stoichiometry and core clustering in native membranes of *Rhodospirillum photometricum*. *EMBO J.* **23**, 4127–4133 (2004).

124. Murugesapillai, D. et al. Accurate nanoscale flexibility measurement of DNA and DNA–protein complexes by atomic force microscopy in liquid. *Nanoscale* **9**, 11327–11337 (2017).

125. Binnig, G., Rohrer, H., Gerber, C. & Weibel, E. 7 × 7 reconstruction on Si(111) resolved in real space. *Phys. Rev. Lett.* **50**, 120–123 (1983).

126. Teichmann, K. et al. Controlled charge switching on a single donor with a scanning tunneling microscope. *Phys. Rev. Lett.* **101**, 076103 (2008).

127. Zheng, H., Weismann, A. & Berndt, R. Manipulation of subsurface donors in ZnO. *Phys. Rev. Lett.* **110**, 226101 (2013).

128. Usman, M. et al. Spatial metrology of dopants in silicon with exact lattice site precision. *Nat. Nanotechnol.* **11**, 763–768 (2016).

129. Kloth, P., Kaiser, K. & Wenderoth, M. Controlling the screening process of a nanoscaled space charge region by minority carriers. *Nat. Commun.* **7**, 10108 (2016).

130. Guo, C. Y. et al. Probing nonequilibrium dynamics of photoexcited polarons on a metal-oxide surface with atomic precision. *Phys. Rev. Lett.* **124**, 206801 (2020).

131. Schofield, S. R. et al. Atomically precise placement of single dopants in Si. *Phys. Rev. Lett.* **91**, 136104 (2003).

132. He, Y. et al. A two-qubit gate between phosphorus donor electrons in silicon. *Nature* **571**, 371–375 (2019).

133. Heinrich, A. J., Lutz, C. P., Gupta, J. A. & Eigler, D. M. Molecule cascades. *Science* **298**, 1381–1387 (2002).

134. Khajetoorians, A. A., Wegner, D., Otte, A. F. & Swart, I. Creating designer quantum states of matter atom-by-atom. *Nat. Rev. Phys.* **1**, 703–715 (2019).

135. Romming, N. et al. Writing and deleting single magnetic skyrmions. *Science* **341**, 636–639 (2013).

136. Ternes, M., Heinrich, A. J. & Schneider, W. D. Spectroscopic manifestations of the Kondo effect on single adatoms. *J. Phys.-Condens. Mat.* **21**, 053001 (2009).

137. Heinrich, B. W., Braun, L., Pascual, J. I. & Franke, K. J. Protection of excited spin states by a superconducting energy gap. *Nat. Phys.* **9**, 765–768 (2013).

138. Nadj-Perge, S. et al. Observation of Majorana fermions in ferromagnetic atomic chains on a superconductor. *Science* **346**, 602–607 (2014).

139. Choi, D. J. et al. Colloquium: atomic spin chains on surfaces. *Rev. Mod. Phys.* **91**, 041001 (2019).

140. Hla, S. W., Bartels, L., Meyer, G. & Rieder, K. H. Inducing all steps of a chemical reaction with the scanning tunneling microscope tip: towards single molecule engineering. *Phys. Rev. Lett.* **85**, 2777–2780 (2000).

141. Meng, X. Z. et al. Direct visualization of concerted proton tunnelling in a water nanocluster. *Nat. Phys.* **11**, 235–239 (2015).

142. Stipe, B. C., Rezaei, M. A. & Ho, W. Single-molecule vibrational spectroscopy and microscopy. *Science* **280**, 1732–1735 (1998).
This article develops IETS, enabling detection of single-molecule vibrations for chemical identification.

143. Stipe, B. C., Rezaei, H. A. & Ho, W. Localization of inelastic tunneling and the determination of atomic-scale structure with chemical specificity. *Phys. Rev. Lett.* **82**, 1724–1727 (1999).

144. Kim, Y., Motobayashi, K., Frederiksen, T., Ueba, H. & Kawai, M. Action spectroscopy for single-molecule reactions—experiments and theory. *Prog. Surf. Sci.* **90**, 85–143 (2015).

145. Lauhon, L. J. & Ho, W. Single molecule thermal rotation and diffusion: acetylene on Cu(001). *J. Chem. Phys.* **111**, 5633–5636 (1999).

146. Pascual, J. I., Lorente, N., Song, Z., Conrad, H. & Rust, H. P. Selectivity in vibrationally mediated single-molecule chemistry. *Nature* **423**, 525–528 (2003).

147. Hahn, J. R. & Ho, W. Oxidation of a single carbon monoxide molecule manipulated and induced with a scanning tunneling microscope. *Phys. Rev. Lett.* **87**, 166102 (2001).

148. Kyriakou, G. et al. Isolated metal atom geometries as a strategy for selective heterogeneous hydrogenations. *Science* **335**, 1209–1212 (2012).

149. Bikondoa, O. et al. Direct visualization of defect-mediated dissociation of water on $TiO_2(110)$. *Nat. Mater.* **5**, 189–192 (2006).

150. Setvin, M. et al. Reaction of O_2 with subsurface oxygen vacancies on TiO_2 anatase (101). *Science* **341**, 988–991 (2013).

151. Li, S. W., Chen, S. Y., Li, J., Wu, R. Q. & Ho, W. Joint space–time coherent vibration driven conformational transitions in a single molecule. *Phys. Rev. Lett.* **119**, 176002 (2017).

152. de Oteyza, D. G. et al. Direct imaging of covalent bond structure in single-molecule chemical reactions. *Science* **340**, 1434–1437 (2013).

153. Gross, L. et al. Measuring the charge state of an adatom with noncontact atomic force microscopy. *Science* **324**, 1428–1431 (2009).

154. Fatayer, S. et al. Molecular structure elucidation with charge-state control. *Science* **365**, 142–145 (2019).

155. Sugimoto, Y. et al. Chemical identification of individual surface atoms by atomic force microscopy. *Nature* **446**, 64–67 (2007).

156. Xu, J. Y. et al. Determining structural and chemical heterogeneities of surface species at the single-bond limit. *Science* **371**, 818–822 (2021).

157. Su, Y. Z., Fu, Y. C., Yan, J. W., Chen, Z. B. & Mao, B. W. Double layer of Au(100)/ionic liquid interface and its stability in imidazolium-based ionic liquids. *Angew. Chem. Int. Edit.* **48**, 5148–5151 (2009).

158. Ye, S., Ishibashi, C. & Uosaki, K. Anisotropic dissolution of an Au(111) electrode in perchloric acid solution containing chloride anion investigated by in situ STM—the important role of adsorbed chloride anion. *Langmuir* **15**, 807–812 (1999).

159. Wu, Z. L. & Yau, S. L. Examination of underpotential deposition of copper on Pt(111) electrodes in hydrochloric acid solutions with in situ scanning tunneling microscopy. *Langmuir* **17**, 4627–4633 (2001).

160. Yoshimoto, S., Higa, N. & Itaya, K. Two-dimensional supramolecular organization of copper octaethylporphyrin and cobalt phthalocyanine on Au(111): molecular assembly control at an electrochemical interface. *J. Am. Chem. Soc.* **126**, 8540–8545 (2004).

161. Fukuma, T., Kimura, M., Kobayashi, K., Matsushige, K. & Yamada, H. Development of low noise cantilever deflection sensor for multienvironment frequency-modulation atomic force microscopy. *Rev. Sci. Instrum.* **76**, 053704 (2005).

162. Ichii, T., Fujimura, M., Negami, M., Murase, K. & Sugimura, H. Frequency modulation atomic force microscopy in ionic liquid using quartz tuning fork sensors. *Jpn. J. Appl. Phys.* **51**, 08KB08 (2012).

163. Purckhauer, K. et al. Imaging in biologically-relevant environments with AFM using stiff qPlus sensors. *Sci. Rep.* **8**, 9330 (2018).

164. Rode, S., Oyabu, N., Kobayashi, K., Yamada, H. & Kuhnle, A. True atomic-resolution imaging of (101̄4) calcite in aqueous solution by frequency modulation atomic force microscopy. *Langmuir* **25**, 2850–2853 (2009).

165. Fukuma, T., Higgins, M. J. & Jarvis, S. P. Direct imaging of lipid-ion network formation under physiological conditions by frequency modulation atomic force microscopy. *Phys. Rev. Lett.* **98**, 106101 (2007).

166. Hiasa, T., Kimura, K. & Onishi, H. Hydration of hydrophilic thiolate monolayers visualized by atomic force microscopy. *Phys. Chem. Chem. Phys.* **14**, 8419–8424 (2012).

167. Martin-Jimenez, D., Chacon, E., Tarazona, P. & Garcia, R. Atomically resolved three-dimensional structures of electrolyte aqueous solutions near a solid surface. *Nat. Commun.* **7**, 12164 (2016).

168. Imada, H., Kimura, K. & Onishi, H. Water and 2-propanol structured on calcite (104) probed by frequency-modulation atomic force microscopy. *Langmuir* **29**, 10744–10751 (2013).

169. Zhong, J. H. et al. Probing the electronic and catalytic properties of a bimetallic surface with 3 nm resolution. *Nat. Nanotechnol.* **12**, 132–136 (2017).

170. Newkome, G. R. et al. Nanoassembly of a fractal polymer: a molecular "Sierpinski hexagonal gasket". *Science* **312**, 1782–1785 (2006).

171. Hussain, H. et al. Structure of a model TiO_2 photocatalytic interface. *Nat. Mater.* **16**, 461–466 (2017).

172. Peng, J. et al. Surface coordination layer passivates oxidation of copper. *Nature* **586**, 390–394 (2020).

173. Balajka, J., Pavelec, J., Komora, M., Schmid, M. & Diebold, U. Apparatus for dosing liquid water in ultrahigh vacuum. *Rev. Sci. Instrum.* **89**, 083906 (2018).

174. Balajka, J. et al. High-affinity adsorption leads to molecularly ordered interfaces on TiO_2 in air and solution. *Science* **361**, 786–788 (2018).

175. Peng, J. B. et al. The effect of hydration number on the interfacial transport of sodium ions. *Nature* **557**, 701–705 (2018).

176. Barth, J. V., Costantini, G. & Kern, K. Engineering atomic and molecular nanostructures at surfaces. *Nature* **437**, 671–679 (2005).

177. Manne, S. & Gaub, H. E. Molecular-organization of surfactants at solid–liquid interfaces. *Science* **270**, 1480–1482 (1995).

178. Holland, N. B., Qiu, Y. X., Ruegsegger, M. & Marchant, R. E. Biomimetic engineering of non-adhesive glycocalyx-like surfaces using oligosaccharide surfactant polymers. *Nature* **392**, 799–801 (1998).

179. Theobald, J. A., Oxtoby, N. S., Phillips, M. A., Champness, N. R. & Beton, P. H. Controlling molecular deposition and layer structure with supramolecular surface assemblies. *Nature* **424**, 1029–1031 (2003).

180. Zhong, D. Y. et al. Linear alkane polymerization on a gold surface. *Science* **334**, 213–216 (2011).

181. Foster, J. S. & Frommer, J. E. Imaging of liquid-crystals using a tunnelling microscope. *Nature* **333**, 542–545 (1988).

182. Ruffieux, P. et al. On-surface synthesis of graphene nanoribbons with zigzag edge topology. *Nature* **531**, 489–492 (2016).

183. Messina, P. et al. Direct observation of chiral metal-organic complexes assembled on a Cu(100) surface. *J. Am. Chem. Soc.* **124**, 14000–14001 (2002).

184. Ma, R. Z. et al. Atomic imaging of the edge structure and growth of a two-dimensional hexagonal ice. *Nature* **577**, 60–63 (2020).

185. Zhang, J. et al. Real-space identification of intermolecular bonding with atomic force microscopy. *Science* **342**, 611–614 (2013).

186. Shang, J. et al. Assembling molecular Sierpinski triangle fractals. *Nat. Chem.* **7**, 389–393 (2015).

187. Han, Z. M. et al. Imaging the halogen bond in self-assembled halogenbenzenes on silver. *Science* **358**, 206–210 (2017).

188. Okawa, Y. & Aono, M. Materials science — nanoscale control of chain polymerization. *Nature* **409**, 683–684 (2001).

189. Muller, W. T. et al. A strategy for the chemical synthesis of nanostructures. *Science* **268**, 272–273 (1995).

190. Cai, J. M. et al. Atomically precise bottom-up fabrication of graphene nanoribbons. *Nature* **466**, 470–473 (2010).

191. Chen, Y. C. et al. Molecular bandgap engineering of bottom-up synthesized graphene nanoribbon heterojunctions. *Nat. Nanotechnol.* **10**, 156–160 (2015).

192. Slota, M. et al. Magnetic edge states and coherent manipulation of graphene nanoribbons. *Nature* **561**, 691–695 (2018).

193. Groning, O. et al. Engineering of robust topological quantum phases in graphene nanoribbons. *Nature* **560**, 209–213 (2018).

194. Rizzo, D. J. et al. Topological band engineering of graphene nanoribbons. *Nature* **560**, 204–208 (2018).

195. Lee, J. et al. Interplay of electron-lattice interactions and superconductivity in Bi$_2$Sr$_2$CaCu$_2$O$_8$$^+$δ. *Nature* **442**, 546–550 (2006).

196. Hess, H. F., Robinson, R. B., Dynes, R. C., Valles, J. M. Jr & Waszczak, J. V. Scanning-tunneling-microscope observation of the Abrikosov flux lattice and the density of states near and inside a fluxoid. *Phys. Rev. Lett.* **62**, 214–216 (1989).

197. Hoffman, J. E. et al. Imaging quasiparticle interference in Bi$_2$Sr$_2$CaCu$_2$O$_8$$^+$δ. *Science* **297**, 1148–1151 (2002).

198. McElroy, K. et al. Relating atomic-scale electronic phenomena to wave-like quasiparticle states in superconducting Bi$_2$Sr$_2$CaCu$_2$O$_8$$^+$δ. *Nature* **422**, 592–596 (2003).

199. Vershinin, M. et al. Local ordering in the pseudogap state of the high-Tc superconductor Bi$_2$Sr$_2$CaCu$_2$O$_8$$^+$δ. *Science* **303**, 1995–1998 (2004).

200. Song, C. L. et al. Direct observation of nodes and twofold symmetry in FeSe superconductor. *Science* **332**, 1410–1413 (2011).

201. Neto, E. H. D. et al. Ubiquitous interplay between charge ordering and high-temperature superconductivity in cuprates. *Science* **343**, 393–396 (2014).

202. Cai, P. et al. Visualizing the evolution from the Mott insulator to a charge-ordered insulator in lightly doped cuprates. *Nat. Phys.* **12**, 1047–1051 (2016).

203. Li, W. et al. Phase separation and magnetic order in K-doped iron selenide superconductor. *Nat. Phys.* **8**, 126–130 (2012).

204. Parker, C. V. et al. Fluctuating stripes at the onset of the pseudogap in the high-Tc superconductor Bi$_2$Sr$_2$CaCu$_2$O$_8$$^+$x. *Nature* **468**, 677–680 (2010).

205. Wise, W. D. et al. Charge-density-wave origin of cuprate checkerboard visualized by scanning tunnelling microscopy. *Nat. Phys.* **4**, 696–699 (2008).

206. Comin, R. et al. Charge order driven by Fermi-arc instability in Bi$_2$Sr$_{2-x}$La$_x$CuO$_6$$^+$δ. *Science* **343**, 390–392 (2014).

207. Hamidian, M. H. et al. Detection of a Cooper-pair density wave in Bi$_2$Sr$_2$CaCu$_2$O$_8$$^+$x. *Nature* **532**, 343–347 (2016).

208. Zhang, T. et al. Experimental demonstration of topological surface states protected by time-reversal symmetry. *Phys. Rev. Lett.* **103**, 266803 (2009).

209. Cheng, P. et al. Landau quantization of topological surface states in Bi$_2$Se$_3$. *Phys. Rev. Lett.* **105**, 076801 (2010).

210. Jiang, Y. P. et al. Landau quantization and the thickness limit of topological insulator thin films of Sb$_2$Te$_3$. *Phys. Rev. Lett.* **108**, 016401 (2012).

211. Beidenkopf, H. et al. Spatial fluctuations of helical Dirac fermions on the surface of topological insulators. *Nat. Phys.* **7**, 939–943 (2011).

212. Okada, Y. et al. Direct observation of broken time-reversal symmetry on the surface of a magnetically doped topological insulator. *Phys. Rev. Lett.* **106**, 206805 (2011).

213. Hor, Y. S. et al. Superconductivity in Cu$_x$Bi$_2$Se$_3$ and its implications for pairing in the undoped topological insulator. *Phys. Rev. Lett.* **104**, 057001 (2010).

214. Okada, Y. et al. Observation of Dirac node formation and mass acquisition in a topological crystalline insulator. *Science* **341**, 1496–1499 (2013).

215. Inoue, H. et al. Quasiparticle interference of the Fermi arcs and surface-bulk connectivity of a Weyl semimetal. *Science* **351**, 1184–1187 (2016).

216. Zhu, S. Y. et al. Nearly quantized conductance plateau of vortex zero mode in an iron-based superconductor. *Science* **367**, 189–192 (2020).

217. Sun, H. H. et al. Majorana zero mode detected with spin selective Andreev reflection in the vortex of a topological superconductor. *Phys. Rev. Lett.* **116**, 257003 (2016).

218. Gomes, K. K., Mar, W., Ko, W., Guinea, F. & Manoharan, H. C. Designer Dirac fermions and topological phases in molecular graphene. *Nature* **483**, 306–310 (2012).

219. Slot, M. R. et al. Experimental realization and characterization of an electronic Lieb lattice. *Nat. Phys.* **13**, 672–676 (2017).

220. Drost, R., Ojanen, T., Harju, A. & Liljeroth, P. Topological states in engineered atomic lattices. *Nat. Phys.* **13**, 668–671 (2017).

221. Zhang, Y. B. et al. Giant phonon-induced conductance in scanning tunnelling spectroscopy of gate-tunable graphene. *Nat. Phys.* **4**, 627–630 (2008).

222. Feng, B. J. et al. Experimental realization of two-dimensional boron sheets. *Nat. Chem.* **8**, 564–569 (2016).

223. Brihuega, I. et al. Quasiparticle chirality in epitaxial graphene probed at the nanometer scale. *Phys. Rev. Lett.* **101**, 206802 (2008).

224. Rutter, G. M. et al. Scattering and interference in epitaxial graphene. *Science* **317**, 219–222 (2007).

225. Chiu, M. H. et al. Determination of band alignment in the single-layer MoS$_2$/WSe$_2$ heterojunction. *Nat. Commun.* **6**, 7666 (2015).

226. Zhang, C. D. et al. Visualizing band offsets and edge states in bilayer–monolayer transition metal dichalcogenides lateral heterojunction. *Nat. Commun.* **7**, 10349 (2016).

227. Zhu, J. Q. et al. Argon plasma induced phase transition in monolayer MoS$_2$. *J. Am. Chem. Soc.* **139**, 10216–10219 (2017).

228. Wang, Z. C. et al. Local engineering of topological phase in monolayer MoS$_2$. *Sci. Bull.* **64**, 1750–1756 (2019).

229. Uri, A. et al. Mapping the twist-angle disorder and Landau levels in magic-angle graphene. *Nature* **581**, 47–52 (2020).

230. Wong, D. L. et al. Cascade of electronic transitions in magic-angle twisted bilayer graphene. *Nature* **582**, 198–202 (2020).

231. Zondiner, U. et al. Cascade of phase transitions and Dirac revivals in magic-angle graphene. *Nature* **582**, 203–208 (2020).

232. Brar, V. W. et al. Gate-controlled ionization and screening of cobalt adatoms on a graphene surface. *Nat. Phys.* **7**, 43–47 (2011).

233. Lee, J. et al. Imaging electrostatically confined Dirac fermions in graphene quantum dots. *Nat. Phys.* **12**, 1032–1036 (2016).

234. Low, T. et al. Polaritons in layered two-dimensional materials. *Nat. Mater.* **16**, 182–194 (2017).

235. Chen, J. N. et al. Optical nano-imaging of gate-tunable graphene plasmons. *Nature* **487**, 77–81 (2012).

236. Chen, W. O. et al. Direct observation of van der Waals stacking-dependent interlayer magnetism. *Science* **366**, 983–987 (2019).

237. Liu, F. C. et al. Room-temperature ferroelectricity in CuInP$_2$S$_6$ ultrathin flakes. *Nat. Commun.* **7**, 12357 (2016).

238. Ohmann, R. et al. Real-space imaging of the atomic structure of organic–inorganic perovskite. *J. Am. Chem. Soc.* **137**, 16049–16054 (2015).

239. Leng, K. et al. Molecularly thin two-dimensional hybrid perovskites with tunable optoelectronic properties due to reversible surface relaxation. *Nat. Mater.* **17**, 908–914 (2018).

240. Hieulle, J. et al. Imaging of the atomic structure of all-inorganic halide perovskites. *J. Phys. Chem. Lett.* **11**, 818–823 (2020).

241. Liu, T. C. et al. In situ quantification of interphasial chemistry in Li-ion battery. *Nat. Nanotechnol.* **14**, 50–56 (2019).

242. Verde, M. G. et al. Elucidating the phase transformation of Li$_4$Ti$_5$O$_{12}$ lithiation at the nanoscale. *ACS Nano.* **10**, 4312–4321 (2016).

243. Eerenstein, W., Mathur, N. D. & Scott, J. F. Multiferroic and magnetoelectric materials. *Nature* **442**, 759–765 (2006).

244. Garcia, V. et al. Giant tunnel electroresistance for non-destructive readout of ferroelectric states. *Nature* **460**, 81–84 (2009).

245. Seidel, J. et al. Conduction at domain walls in oxide multiferroics. *Nat. Mater.* **8**, 229–234 (2009).

246. Zhao, T. et al. Electrical control of antiferromagnetic domains in multiferroic BiFeO$_3$ films at room temperature. *Nat. Mater.* **5**, 823–829 (2006).

247. Lu, H. et al. Mechanical writing of ferroelectric polarization. *Science* **336**, 59–61 (2012).

248. Jesse, S. et al. Direct imaging of the spatial and energy distribution of nucleation centres in ferroelectric materials. *Nat. Mater.* **7**, 209–215 (2008).

249. Gruverman, A., Wu, D. & Scott, J. F. Piezoresponse force microscopy studies of switching behavior of ferroelectric capacitors on a 100-ns time scale. *Phys. Rev. Lett.* **100**, 097601 (2008).

250. Geng, Y. N., Lee, N., Choi, Y. J., Cheong, S. W. & Wu, W. D. Collective magnetism at multiferroic vortex domain walls. *Nano Lett.* **12**, 6055–6059 (2012).

251. Gross, I. et al. Real-space imaging of non-collinear antiferromagnetic order with a single-spin magnetometer. *Nature* **549**, 252–256 (2017).

252. Muller, D. J. & Engel, A. Voltage and pH-induced channel closure of porin OmpF visualized by atomic force microscopy. *J. Mol. Biol.* **285**, 1347–1351 (1999).

253. Mulvihill, E. et al. Mechanism of membrane pore formation by human gasdermin-D. *EMBO J.* **37**, e98321 (2018).

254. Leung, C. et al. Atomic force microscopy with nanoscale cantilevers resolves different structural conformations of the DNA double helix. *Nano. Lett.* **12**, 3846–3850 (2012).

255. Pasquina-Lemonche, L. et al. The architecture of the Gram-positive bacterial cell wall. *Nature* **582**, 294–297 (2020).
This AFM article brings exciting new insight into the architecture of bacterial cell walls.

256. Engel, A. & Muller, D. J. Observing single biomolecules at work with the atomic force microscope. *Nat. Struct. Biol.* **7**, 715–718 (2000).

257. Matzke, R., Jacobson, K. & Radmacher, M. Direct, high-resolution measurement of furrow stiffening during division of adherent cells. *Nat. Cell Biol.* **3**, 607–610 (2001).

258. Cisneros, D. A., Hung, C., Franz, C. A. & Muller, D. J. Observing growth steps of collagen self-assembly by time-lapse high-resolution atomic force microscopy. *J. Struct. Biol.* **154**, 232–245 (2006).

259. Viani, M. B. et al. Probing protein–protein interactions in real time. *Nat. Struct. Biol.* **7**, 644–647 (2000).

260. Muller, D. J. & Engel, A. Conformations, flexibility, and interactions observed on individual membrane proteins by atomic force microscopy. *Methods Cell Biol.* **68**, 257–299 (2002).

261. Mari, S. A. et al. Gating of the MlotiK1 potassium channel involves large rearrangements of the cyclic nucleotide-binding domains. *Proc. Natl Acad. Sci. USA* **108**, 20802–20807 (2011).

262. Koster, D. A., Croquette, V., Dekker, C., Shuman, S. & Dekker, N. H. Friction and torque govern the relaxation of DNA supercoils by eukaryotic topoisomerase IB. *Nature* **434**, 671–674 (2005).

263. Kodera, N., Yamamoto, D., Ishikawa, R. & Ando, T. Video imaging of walking myosin V by high-speed atomic force microscopy. *Nature* **468**, 72–76 (2010). **This article on high-speed AFM demonstrates direct imaging of a single motor protein at work**.

264. Eskandarian, H. A. et al. Division site selection linked to inherited cell surface wave troughs in mycobacteria. *Nat. Microbiol.* **2**, 17094 (2017).

265. Shibata, M., Yamashita, H., Uchihashi, T., Kandori, H. & Ando, T. High-speed atomic force microscopy shows dynamic molecular processes in photoactivated bacteriorhodopsin. *Nat. Nanotechnol.* **5**, 208–212 (2010).

266. Preiner, J. et al. IgGs are made for walking on bacterial and viral surfaces. *Nat. Commun.* **5**, 4394 (2014).

267. Uchihashi, T., Iino, R., Ando, T. & Noji, H. High-speed atomic force microscopy reveals rotary catalysis of rotorless F$_1$-ATPase. *Science* **333**, 755–758 (2011).

268. Chiaruttini, N. et al. Relaxation of loaded ESCRT-III spiral springs drives membrane deformation. *Cell* **163**, 866–879 (2015).

269. Sakiyama, Y., Mazur, A., Kapinos, L. E. & Lim, R. Y. H. Spatiotemporal dynamics of the nuclear pore complex transport barrier resolved by high-speed atomic force microscopy. *Nat. Nanotechnol.* **11**, 719–723 (2016).

270. Ruan, Y. et al. Direct visualization of glutamate transporter elevator mechanism by high-speed AFM. *Proc. Natl Acad. Sci. USA* **114**, 1584–1588 (2017).

271. Shibata, M. et al. Real-space and real-time dynamics of CRISPR–Cas9 visualized by high-speed atomic force microscopy. *Nat. Commun.* **8**, 1430 (2017).

272. Heath, G. R. & Scheuring, S. High-speed AFM height spectroscopy reveals µs-dynamics of unlabeled biomolecules. *Nat. Commun.* **9**, 4983 (2018).

273. Muller, D. J., Buldt, G. & Engel, A. Force-induced conformational change of bacteriorhodopsin. *J. Mol. Biol.* **249**, 239–243 (1995).

274. Lin, Y. C. et al. Force-induced conformational changes in PIEZO1. *Nature* **573**, 230–234 (2019).

275. Hansma, H. G. et al. Reproducible imaging and dissection of plasmid DNA under liquid with the atomic force microscope. *Science* **256**, 1180–1184 (1992).

276. Hoh, J. H., Lal, R., John, S. A., Revel, J. P. & Arnsdorf, M. F. Atomic force microscopy and dissection of gap-junctions. *Science* **253**, 1405–1408 (1991).

277. Alsteens, D. et al. Atomic force microscopy-based characterization and design of biointerfaces. *Nat. Rev. Mater.* **2**, 17008 (2017).

278. Viani, M. B. et al. Fast imaging and fast force spectroscopy of single biopolymers with a new atomic force microscope designed for small cantilevers. *Rev. Sci. Instrum.* **70**, 4300–4303 (1999).

279. Miyagi, A. & Scheuring, S. Automated force controller for amplitude modulation atomic force microscopy. *Rev. Sci. Instrum.* **87**, 053705 (2016).

280. Janshoff, A., Neitzert, M., Oberdorfer, Y. & Fuchs, H. Force spectroscopy of molecular systems — single molecule spectroscopy of polymers and biomolecules. *Angew. Chem. Int. Edit.* **39**, 3213–3237 (2000).

281. Muller, D. J., Helenius, J., Alsteens, D. & Dufrene, Y. F. Force probing surfaces of living cells to molecular resolution. *Nat. Chem. Biol.* **5**, 383–390 (2009).

282. Schillers, H. et al. Standardized nanomechanical atomic force microscopy procedure (SNAP) for measuring soft and biological samples. *Sci. Rep.* **7**, 5117 (2017).

283. Lomakin, A. J. et al. The nucleus acts as a ruler tailoring cell responses to spatial constraints. *Science* **370**, 310–322 (2020).

284. Stewart, M. P. et al. Hydrostatic pressure and the actomyosin cortex drive mitotic cell rounding. *Nature* **469**, 226–230 (2011). **This article unravels the biological mechanism of how mammalian cells round up to enter mitosis and divide**.

285. Ramanathan, S. P. et al. Cdk1-dependent mitotic enrichment of cortical myosin II promotes cell rounding against confinement. *Nat. Cell Biol.* **17**, 148–159 (2015).

286. Medalsy, I. D. & Muller, D. J. Nanomechanical properties of proteins and membranes depend on loading rate and electrostatic interactions. *ACS Nano.* **7**, 2642–2650 (2013).

287. Rigato, A., Miyagi, A., Scheuring, S. & Rico, F. High-frequency microrheology reveals cytoskeleton dynamics in living cells. *Nat. Phys.* **13**, 771–775 (2017).

288. Moy, V. T., Florin, E. L. & Gaub, H. E. Intermolecular forces and energies between ligands and receptors. *Science* **266**, 257–259 (1994).

289. Milles, L. F., Schulten, K., Gaub, H. E. & Bernardi, R. C. Molecular mechanism of extreme mechanostability in a pathogen adhesin. *Science* **359**, 1527–1532 (2018).

290. Evans, E. A. & Calderwood, D. A. Forces and bond dynamics in cell adhesion. *Science* **316**, 1148–1153 (2007).

291. Friddle, R. W., Noy, A. & De Yoreo, J. J. Interpreting the widespread nonlinear force spectra of intermolecular bonds. *Proc. Natl Acad. Sci. USA* **109**, 13573–13578 (2012).

292. Benoit, M., Gabriel, D., Gerisch, G. & Gaub, H. E. Discrete interactions in cell adhesion measured by single-molecule force spectroscopy. *Nat. Cell Biol.* **2**, 313–317 (2000).

293. Helenius, J., Heisenberg, C. P., Gaub, H. E. & Muller, D. J. Single-cell force spectroscopy. *J. Cell Sci.* **121**, 1785–1791 (2008).

294. Alsteens, D. et al. Nanomechanical mapping of first binding steps of a virus to animal cells. *Nat. Nanotechnol.* **12**, 177–183 (2017).

295. Lang, H. P. & Gerber, C. Microcantilever sensors. *Top. Curr. Chem.* **285**, 1–27 (2008).

296. McKendry, R. et al. Multiple label-free biodetection and quantitative DNA-binding assays on a nanomechanical cantilever array. *Proc. Natl Acad. Sci. USA* **99**, 9783–9788 (2002). **This pioneering microcantilever-based work directly detects the binding of complementary strands of DNA**.

297. Burg, T. P. et al. Weighing of biomolecules, single cells and single nanoparticles in fluid. *Nature* **446**, 1066–1069 (2007).

298. Martinez-Martin, D. et al. Inertial picobalance reveals fast mass fluctuations in mammalian cells. *Nature* **550**, 500–505 (2017).

299. Sader, J. E., Chon, J. W. M. & Mulvaney, P. Calibration of rectangular atomic force microscope cantilevers. *Rev. Sci. Instrum.* **70**, 3967–3969 (1999).

300. Sader, J. E. et al. A virtual instrument to standardise the calibration of atomic force microscope cantilevers. *Rev. Sci. Instrum.* **87**, 093711 (2016).

301. Staudacher, T. et al. Nuclear magnetic resonance spectroscopy on a (5-nanometer)^3 sample volume. *Science* **339**, 561–563 (2013).

302. Besenbacher, F., Laegsgaard, E. & Stensgaard, I. Fast-scanning STM studies. *Mater. Today* **8**, 26–30 (2005).

303. Garg, M. & Kern, K. Attosecond coherent manipulation of electrons in tunneling microscopy. *Science* **367**, 411–415 (2020).

304. Albrektsen, O., Arent, D. J., Meier, H. P. & Salemink, H. W. M. Tunneling microscopy and spectroscopy of molecular-beam epitaxy grown GaAs–AlGaAs interfaces. *Appl. Phys. Lett.* **57**, 31–33 (1990).

305. Kehr, S. C. et al. Near-field examination of perovskite-based superlenses and superlens-enhanced probe–object coupling. *Nat. Commun.* **2**, 249 (2011).

306. Gruber, A. et al. Scanning confocal optical microscopy and magnetic resonance on single defect centers. *Science* **276**, 2012–2014 (1997).

307. Taylor, J. M. et al. High-sensitivity diamond magnetometer with nanoscale resolution. *Nat. Phys.* **4**, 810–816 (2008).

308. Thiel, L. et al. Quantitative nanoscale vortex imaging using a cryogenic quantum magnetometer. *Nat. Nanotechnol.* **11**, 677–681 (2016).

309. Thiel, L. et al. Probing magnetism in 2D materials at the nanoscale with single-spin microscopy. *Science* **364**, 973–976 (2019).

310. Bian, K. et al. Nanoscale electric-field imaging based on a quantum sensor and its charge-state control under ambient condition. *Nat. Commun.* **12**, 2457 (2021).

311. Schouteden, K. et al. Probing the atomic structure of metallic nanoclusters with the tip of a scanning tunneling microscope. *Nanoscale* **6**, 2170–2176 (2014).

312. Umeda, K. et al. Atomic-resolution three-dimensional hydration structures on a heterogeneously charged surface. *Nat. Commun.* **8**, 093706 (2017).

313. Moreno, C., Stetsovych, O., Shimizu, T. K. & Custance, O. Imaging three-dimensional surface objects with submolecular resolution by atomic force microscopy. *Nano. Lett.* **15**, 2257–2262 (2015).

314. Iwata, K. et al. Chemical structure imaging of a single molecule by atomic force microscopy at room temperature. *Nat. Commun.* **6**, 7766 (2015).

315. Alldritt, B. et al. Automated structure discovery in atomic force microscopy. *Sci. Adv.* **6**, eaay6913 (2020).

316. Grinolds, M. S. et al. Subnanometre resolution in three-dimensional magnetic resonance imaging of individual dark spins. *Nat. Nanotechnol.* **9**, 279–284 (2014).

317. Gil-Santos, E. et al. Optomechanical detection of vibration modes of a single bacterium. *Nat. Nanotechnol.* **15**, 469–474 (2020).

318. Frenken, J. W. M., Hamers, R. J. & Demuth, J. E. Thermal roughening studied by scanning tunneling microscopy. *J. Vac. Sci. Technol. A* **8**, 293–296 (1990).

319. Rico, F., Gonzalez, L., Casuso, I., Puig-Vidal, M. & Scheuring, S. High-speed force spectroscopy unfolds titin at the velocity of molecular dynamics simulations. *Science* **342**, 741–743 (2013).

320. Yu, H., Siewny, M. G. W., Edwards, D. T., Sanders, A. W. & Perkins, T. T. Hidden dynamics in the unfolding of individual bacteriorhodopsin proteins. *Science* **355**, 945–949 (2017).

321. Oesterhelt, F. et al. Unfolding pathways of individual bacteriorhodopsins. *Science* **288**, 143–146 (2000).

322. Raab, A. et al. Antibody recognition imaging by force microscopy. *Nat. Biotechnol.* **17**, 902–905 (1999).

323. Ebner, A., Wildling, L. & Gruber, H. J. Functionalization of AFM tips and supports for molecular recognition force spectroscopy and recognition imaging. *Methods Mol. Biol.* **1886**, 117–151 (2019).

324. Hinterdorfer, P., Baumgartner, W., Gruber, H. J., Schilcher, K. & Schindler, H. Detection and localization of individual antibody–antigen recognition events by atomic force microscopy. *Proc. Natl Acad. Sci. USA* **93**, 3477–3481 (1996).

325. Schoeler, C. et al. Ultrastable cellulosome–adhesion complex tightens under load. *Nat. Commun.* **5**, 5635 (2014).

326. Alsteens, D., Trabelsi, H., Soumillion, P. & Dufrene, Y. F. Multiparametric atomic force microscopy imaging of single bacteriophages extruding from living bacteria. *Nat. Commun.* **4**, 2926 (2013).

327. Alsteens, D., Garcia, M. C., Lipke, P. N. & Dufrene, Y. F. Force-induced formation and propagation of adhesion nanodomains in living fungal cells. *Proc. Natl Acad. Sci. USA* **107**, 20744–20749 (2010).

328. Alsteens, D. et al. Imaging G protein-coupled receptors while quantifying their ligand-binding free-energy landscape. *Nat. Methods* **12**, 845–851 (2015).

329. Pfreundschuh, M. et al. Identifying and quantifying two ligand-binding sites while imaging native human membrane receptors by AFM. *Nat. Commun.* **6**, 8857 (2015).

Author contributions

All authors read and edited the full article. Introduction (K.B. and Y.J.); Experimentation (K.B., C.G., A.J.H., D.J.M. and Y.J.); Results (S.S.); Application (K.B., C.G., A.J.H., D.J.M. and Y.J.); Reproducibility and data deposition (S.S.); Limitations and optimizations (Y.J.); Outlook (C.G., D.J.M. and Y.J.); Overview of the Primer (K.B. and Y.J.). With the exception of Y.J., all authors are listed alphabetically.

Competing interests

The authors declare no competing interests.

Peer review information

Nature Reviews Methods Primers thanks Y. Kim, C. Mueller-Renno, J. Xu, C. Ziegler and the other, anonymous, reviewer(s) for their contribution to the peer review of this work.

Publisher's note

Springer Nature remains neutral with regard to jurisdictional claims in published maps and institutional affiliations.

RELATED LINKS
ImageJ: https://imagej.nih.gov/ij/